Modeling the TDFD dissolution of Al-Fe-Mn-Si particles in an Al-4.5Zn-1Mg alloy

Ali Reza Eivani, Hany Ahmed, Jie Zhou, Jurek Duszczyk

Modeling the TDFD dissolution of Al-Fe-Mn-Si particles in an Al-4.5Zn-1Mg alloy

Journal:	*Philosophical Magazine & Philosophical Magazine Letters*
Manuscript ID:	TPHM-09-Sep-0413.R1
Journal Selection:	Philosophical Magazine
Date Submitted by the Author:	18-Jan-2010
Complete List of Authors:	Eivani, Ali Reza; Delft University of Technology, materials Science Engineering Ahmed, Hany; M2i, LMP Zhou, Jie; Delft University of Technology, Materials Science Engineering Duszczyk, Jurek; Delft University of Technology, Materials Science Engineering
Keywords:	aluminium alloys, intermetallic compounds
Keywords (user supplied):	Al-Fe-Mn-Si particles, modeling, dissolution

Modeling the TDFD dissolution of Al-Fe-Mn-Si particles in an Al-4.5Zn-1Mg alloy

A.R. Eivani [1,2] *, H. Ahmed [1], J. Zhou [2], J. Duszczyk [2]

[1] Materials Innovation Institute (M2i), Mekelweg 2, 2628 CD Delft, the Netherlands

[2] Department of Materials Science and Engineering, Delft University of Technology, Mekelweg 2, 2628 CD Delft, the Netherlands

Abstract

Dissolution of large particles in DC-cast 7xxx aluminum alloys is one of the primary objectives of the homogenization process. A mathematical model to describe and predict this complex thermodynamical and kinetical process is of great significance. In this paper, the details of a diffusion limited dissolution model developed based on the thinning, discontinuation and full dissolution (TDFD) mechanism to predict the dissolution of the $Al_{17}(Fe_{3.2},Mn_{0.8})Si_2$ particles are described. The model is capable of predicting the volume fraction and the thickness of the particles during homogenization at different temperatures and time intervals. The predicted results are in good agreement with the measurements using quantitative X-ray diffraction (QXRD) and quantitative field emission gun-scanning electron microscopy (QSEM). The model predictions of the supersaturation parameter, interface position, interface movement rate of the planar surfaces and the cylindrical edges, and the effect of the occurrence of discontinuities on the dissolution extent are presented.

Keywords: Al-4.5Zn-1Mg alloy; modeling; dissolution; intermetallic compounds; analytical methods.

* Corresponding author, PhD researcher, Email: a.r.eivani@tudelft.nl, a.eivani@m2i.nl,

Tel: +31 (0) 15 278 22 02, Fax: +31 (0) 15 278 67 30.

1. Introduction

Homogenization treatment is an important industrial process applied to direct chill (DC) cast aluminum alloys that are subsequently subjected to deformation. It is carried out to improve their final mechanical properties and also to facilitate the subsequent processing towards the final product. It aims at redistributing the alloying elements on a micro scale [1, 2] and dissolving the detrimental particles such as those with low melting points [1, 2] or those which will deteriorate the deformability during hot deformation [3].

In the case of the AA7020 aluminum alloy, more than 70% of the constitutive particles are composed of the $Al_{17}(Fe_{3.2},Mn_{0.8})Si_2$ phase [4], elongated alongside the grain boundaries (GB). It is well known that the presence of second-phase particles can deteriorate the mechanical properties and hot deformability of the alloy, especially if these are located in the grain boundary regions [5-9]. Therefore, the dissolution of these particles during the homogenization of DC-cast AA7020 aluminum billets is of prime importance. The optimization of the homogenization process in terms of the dissolution of these particles requires a fundamental understanding of the dissolution mechanism, which has recently been proposed and termed thinning, discontinuation and full dissolution (TDFD) [4]. In this mechanism, the dissolution process starts with the thinning of the particles. The thinning process continues until the particles become discontinuous in some regions and finally the full dissolution of particles occurs. It is of interest to develop a model that correlates characteristic parameters of the particles such as concentrations, sizes, shapes and geometries with dissolution temperature and holding time. To author's best knowledge, the dissolution of the $Al_{17}(Fe_{3.2},Mn_{0.8})Si_2$ particles based on the TDFD mechanism has not been mathematically expressed.

In the past, particle dissolution in general has been studied by numerous

researchers using a variety of analytical and numerical techniques [10-32]. For example, Aaron and Kotler [10] investigated the effects of the diffusion of the elements in the matrix, interfacial reactions and the curvatures of the particles on the dissolution of precipitates in binary alloys. It was found that the presence of curvature tended to accelerate the dissolution, being particularly important at long times (i.e., when precipitate sizes become small) and when the difference between the solute concentration at the precipitate/matrix interface and in the depleted matrix was small. It was shown, however, that curvature would not affect the dissolution kinetics significantly even at long times unless the concentration difference between the particle/matrix interface and the matrix was sufficiently small. The interface reaction kinetics might produce significant alterations in the dissolution kinetics and increase the total time needed for dissolution. It was also found that for the uniform detachment mechanism, the interface reaction would have no sensible effect when the kinetics coefficient (K_o) was larger than 10^{-3} cm/sec. On the other hand, when $K_o<10^{-7}$ cm/sec, the particle would be effectively insoluble due to the extremely sluggish kinetics. Whelan [11] performed a similar analysis for perfectly spherical precipitates. Both Aaron and Kotler [10] and Whelan [11] developed analytical expressions to quantify the radius of a spherical dissolving precipitate in a binary alloy in an infinite domain. Nolfi et al. [12] used the separation of variables method to solve the kinetic problem of the dissolution and growth of a spheroidized, solute-rich stoichiometric precipitate in the surrounding matrix. The applicability of this method to solve the dissolution and growth problems was demonstrated. Tanzilli and Heckel [13] solved the diffusion equation numerically using a finite difference technique for the spherical particles with a constant radius. Tundal and Ryum [14, 15] considered the effect of the size distribution of particles on their dissolution during homogenization. The results demonstrated that the

distribution of particle sizes was indeed an effective parameter on the model predictions and therefore should be considered in the model if an accurate prediction of the dissolution kinetics was to be achieved. In addition, Vermolen and Vuik [16, 17] presented a mathematical model with nonlinear boundary conditions at the interface and compared the numerical solution with the solutions obtained by the analytical methods. A better agreement between the numerical solution and experimental results was found. Nojiri and Enomoto [18] attempted to reach an exact diffusion controlled dissolution solution for spherical precipitates. By applying their formalism the incorporation of the influence of capillarity on the dissolution kinetics into the model became possible. Aaron et al. [19] compared different mathematical approximations, i.e., interval field (Laplace), the invariant size (stationary interface), linearized gradient and the reversed growth in diffusion limited phase transformations. They found that the stationary interface was the best approximation. Sinder and Pelleg [20] presented the same solution as Aaron et al., [19] for planar and spherical particles and compared the results related to these different situations. The effect of cross-diffusion in multi-component alloys on the dissolution of particles of different geometries; i.e., cylindrical, spherical and planar was modeled by Vermolen et al. [21]. In more recent studies, dissolution models were extended to multi-component systems in one dimension and to binary systems in two dimensions [22-32] and a better agreement between the experimental and predicted results was achieved.

All of the previously published models are limited to a specific geometry, i.e., spherical, cylindrical or planar geometry. These do not consider a combined mode of dissolution from the surfaces and the edges of plate-like particles. However, in the real particle dissolution process, the element flux from all free surfaces of particles, especially that from edges where there are increases in the concentrations of elements at

the particle/matrix interface due to the curvature, is of great importance. Generally, due to the large surfaces of plate-like particles compared with their edges, at the onset of the dissolution process, the fraction of dissolution from the edges relative to that from the planar surfaces is insignificant. Therefore, in a general mode for dissolution from the planar surfaces of a plate-like particle at the beginning of dissolution, neglecting the effect of dissolution from the edges may be allowed. However, as the dissolution proceeds further, the fraction of the dissolution from the edges relative to that from the planar surfaces increases as the radius of the edges decreases and consequently the supersaturation in the vicinity of the particle increases significantly. A larger dissolution rate of particles from the edges than that from planar surfaces was proven by Aaron and Kotler [10] in the case of spherical precipitates dissolving in an infinite matrix. It was found that as time increased, the volume for mass transfer increased, which accelerated the dissolution process. This condition resembles that occurring at the edges of a plate-like particle where the decrease in the thickness of the particle and consequently the decrease in the radius of the edges result in a larger dissolution rate from the edges. This is different from the planar case because the volume of the mass transferred ahead of the moving interface is always constant.

Experimental observations [4] have shown that some of the particles dissolve with a mechanisms different than those known in the literature, which makes the modeling of the dissolution process quite complicated. In the case of $Al_{17}(Fe_{3.2},Mn_{0.8})Si_2$ particles in the AA7020 aluminum alloy, dissolution occurs through the TDFD mechanism [4]. This mechanism is unique and the existing models are not applicable. The TDFD mechanism takes an increase in the number density of the edges of the particles in the structure into account. Therefore, considering the effect of the dissolution from the edges of the particles is essential for the model.

The objective of the research was to develop a model based on the TDFD dissolution mechanism, which could be used to predict the volume fraction of the $Al_{17}(Fe_{3.2},Mn_{0.8})Si_2$ particles dissolved during the homogenization process. The research was focused on the dissolution of the $Al_{17}(Fe_{3.2},Mn_{0.8})Si_2$ particles in the AA7020 aluminum alloy which, in spite of its practical importance, has received little attention in the research community. The predictions were verified experimentally by using FEG-SEM analysis and quantitative XRD analysis.

2. The model

2.1. The TDFD dissolution mechanism

The dissolution mechanism of a $Al_{17}(Fe_{3.2},Mn_{0.8})Si_2$ particle at various stages of homogenization is schematically illustrated in Fig. 1. Fig. 1 (a-d) shows the overall thinning process of the $Al_{17}(Fe_{3.2},Mn_{0.8})Si_2$ particle. In Fig. 1 (e) the formation of discontinuities is shown. Assuming that during homogenization an overall decrease in the width of the $Al_{17}(Fe_{3.2},Mn_{0.8})Si_2$ particle occurs at a constant rate in different regions regardless of the width (Fig. 1 (a-d)), the parts having smaller widths become thinner than the other parts and meet each other sooner, as shown in Fig. 1 (d) and (e). Therefore, the discontinuities (Fig. 1 (f)) occur as a result of the inherent perturbations of the surfaces of the $Al_{17}(Fe_{3.2},Mn_{0.8})Si_2$ particle [4]. At the end of the process, the full dissolution of the particles continues with the thinning of the remaining parts and theformation of new discontinuities, if there are still remaining perturbations.

2.2. Model setup and assumptions

A model based on the TDFD dissolution mechanism [4] has been developed to predict the dissolution of the $Al_{17}(Fe_{3.2},Mn_{0.8})Si_2$ particles in AA7020 during homogenization. This model is capable of predicting the volume fraction and the

thickness of the particles during homogenization at different temperatures and times. In this model, the particle is considered to be a two dimensional plate with round cylindrical edges and initial perturbations on the planar surfaces located alongside the grain boundaries.

The dissolution of the particle occurs from surfaces and cylindrical edges into the grain interior, as shown in Fig. 2. During dissolution, discontinuities occur at the initially thinner parts of the particle, leading to an increase in the number density of the cylindrical edges, as shown schematically in Fig. 1 (a) through (f).

The application of this modeling framework to the dissolution of $Al_{17}(Fe_{3.2},Mn_{0.8})Si_2$ particles requires the following simplifications:

- The dissolution of an isolated particle into an infinite matrix in two dimensions is considered a diffusion-limited process. The influence of interface reactions on the dissolution is neglected. The diffusion rate of the slowest diffusing element, in this case Mn [33], is considered the controlling factor of dissolution rate. Moreover, the diffusion coefficient is assumed to be independent of composition.

- The solute concentrations in the precipitate are constant and equal to their equilibrium values [10, 15-20]. The solute concentrations are assumed to be independent of the distance from the precipitate/matrix interface and temperature. In other words, there are no concentration gradients in the particle [10, 15-20]. Moreover, the diffusion coefficients of the elements in the particle are negligibly small compared to the diffusion coefficients in the matrix.

- Discontinuities in the TDFD dissolution mechanism [4] may occur as a geometrical issue as well as due to heterogeneous distributions of solute atoms. From experimental observations as presented elsewhere [4], the discontinuities occur mainly due to the

initial perturbations on the surfaces of the particles. The heterogeneous distribution of solute atoms can accelerate them.

- The dissolution occurs on the planar surfaces and the cylindrical edges of the particle. The dissolution from the tapered surfaces between the perturbations and the particle bulk (Fig. 3) is neglected.

- The effect of the initial concentrations of the elements in the structure, before dissolution, is incorporated into the system; however, the effect of solidification segregation is neglected [10, 15-20]. During dissolution, due to the increases in the concentrations of the elements in the surrounding matrix, the dissolution rate decreases. The change in the composition of the matrix due to dissolution is also included in the model by considering an average concentration after each individual time step. The total time of homogenization is composed of small time steps and, at each time step, the increase in the concentration of the matrix due to the dissolution is updated.

- Diffusion along the grain boundaries is important at low temperatures but not at high temperatures, i.e., $T > 0.5T_m$ [34]. This is due to exponential increase in the number density of vacancies at high temperatures which controls the diffusion rate. Temperature range used in this research, i.e., between 390 and 550 °C, is significantly higher than $0.5T_m$. Therefore, it is reasonable to assume that during homogenization there is no effect of the grain boundaries on the increases of the diffusion rates of the elements, even though the $Al_{17}(Fe_{3.2},Mn_{0.8})Si_2$ particles are located at the grain boundaries.

- During dissolution, the particle has a finite, nonzero initial width and the cylindrical edge radii are instantaneously equal to its half-thickness, which is a geometrically necessary condition (GNC) as will be discussed later. The particle decreases its size by transferring (or rejecting) solutes into the matrix behind the thinning interface.

2.2. The dissolution process

2.2.1. Dissolution from the planar surfaces

The dissolution from the planar surfaces of the particles may be simplified as the dissolution of a one-dimensional plate-like particle. Assuming the diffusion-limited character for the dissolution of the particle, one arrives at the following equation [10];

$$D\nabla^2 C(x,t) = \frac{\partial C(x,t)}{\partial t} \tag{1}$$

where D is the volume diffusion coefficient in the matrix and $C(x,t)$ the concentration field surrounding the particle. The initial and boundary conditions are described in the following equation [10]

$$\begin{aligned} &C(x,t=0) = C_{\mathrm{M}} && x \geq S_0 \\ &C(x=S_0,t) = C_{\mathrm{Ip}} && 0 < t < \infty \\ &C(x=\infty,t) = C_{\mathrm{M}} && 0 \leq t \leq \infty \end{aligned} \tag{2}$$

where x is equal to S_0 at the particle/matrix interface and C_{Ip} and C_{M} are the concentrations of the elements at the particle/matrix interface and in the matrix, respectively. The term S_0 denotes the value of S at t=0. Considering a flux balance at the particle/matrix interface, one can write [10]

$$\left(C_{\mathrm{P}} - C_{\mathrm{Ip}}\right)\frac{dS}{dt} = D\left(\frac{\partial C}{\partial x}\right) \qquad x = S \tag{3}$$

where C_{P}, the concentration of the diffusing element in the particle, is considered a constant independent of x and t. The analytical solution of Eq. (1) with the initial and boundary conditions presented in Eqs. (2) and (3) for a plate-like particle is known [10, 19]. Using the exact solution to calculate the thickness of the dissolving particle, one may express [10, 19]:

$$S = S_0 - \lambda_{\mathrm{p}}\sqrt{Dt} \tag{4}$$

for

$$\sqrt{\pi}\lambda_{\mathrm{p}} \exp\left(\frac{\lambda_{\mathrm{p}}^{2}}{4}\right) erfc\left(-\frac{\lambda_{\mathrm{p}}}{2}\right) = k_{\mathrm{p}} \tag{5}$$

where k_{p}, the supersaturation parameter of the planar surfaces, is defined as

$$k_{\mathrm{p}} = 2\frac{\left(C_{\mathrm{Ip}} - C_{\mathrm{M}}\right)}{\left(C_{\mathrm{P}} - C_{\mathrm{Ip}}\right)} \tag{6}$$

When k is small [10, 19],

$$\lambda_{\mathrm{p}} = \frac{k_{\mathrm{p}}}{\sqrt{\pi}} \tag{7}$$

which can be written as

$$\lambda_{\mathrm{p}} = \frac{2}{\sqrt{\pi}}\frac{\left(C_{\mathrm{Ip}} - C_{\mathrm{M}}\right)}{\left(C_{\mathrm{P}} - C_{\mathrm{Ip}}\right)} \tag{8}$$

In this case, the time for full dissolution of the particle (t_{f}) and for reaching the width of the particle to the half of its initial value (t_{h}) can be determined as Eqs. (9) and (10) respectively.

$$t_f = \frac{\pi}{4D}\left(S_0\frac{\left(C_{\mathrm{P}} - C_{\mathrm{Ip}}\right)}{\left(C_{\mathrm{Ip}} - C_{\mathrm{M}}\right)}\right)^2 \tag{9}$$

$$t_h = \frac{\pi}{16D}\left(S_0\frac{\left(C_{\mathrm{P}} - C_{\mathrm{Ip}}\right)}{\left(C_{\mathrm{Ip}} - C_{\mathrm{M}}\right)}\right)^2 \tag{10}$$

t_{h} will be used as a boundary condition for the dissolution from the cylindrical edges which will be explained later.

Using the exact solution, the chemical composition of the matrix can be calculated using Eq. (11) [10]

$$C(x,t) = (C_{Ip} - C_M)\frac{erfc\left((x - S_0)/2\sqrt{Dt}\right)}{erfc(\lambda_P)} + C_M \quad (11)$$

2.2.2. Dissolution from the cylindrical edges

As shown in Fig. 3, the dissolution from the cylindrical edges is, in fact, the dissolution of a cylindrical surface. Therefore, the dissolution has been modeled, considering the dissolution of a one dimensional circle with axial symmetry. In this case, Eqs. (1) through (3) can be written as [35];

$$\frac{\partial C(r,t)}{\partial t} = D\left(\frac{\partial^2 C(r,t)}{\partial r^2} + \frac{1}{r}\frac{\partial C(r,t)}{\partial r}\right) \quad (12)$$

where $C(r,t)$ is the concentration field surrounding the particle subject to the conditions;

$$\begin{aligned} &C(r,t=0) = C_M && r \geq R_0 \\ &C(r=R,t) = C_{It} && 0 < t < \infty \\ &C(r=\infty,t) = C_M && 0 \leq t \leq \infty \end{aligned} \quad (13)$$

where $r=R$ is at the particle/matrix interface. The term R_0 denotes the value of R at $t=0$. C_{It} is the concentration of the matrix at the particle/matrix interface including the effect of the curvature of the particle. The other parameters have the same definitions as in Eqs. (1) through (3).

The effect of the curvature of the particle on the change in the concentration field can be imported into the model using the Gibbs-Thompson equation modified by Hillert [36] who showed that the composition in the matrix at the curved particle/matrix interface (C_{It}) varied with particle radius, R, as described in Eq. (14)

$$C_{It} = C_I(\infty)\exp\left(\frac{2\gamma V_P}{R_g T}\frac{1}{R}\right) \quad (14)$$

where $C_I(\infty)$ is the mean matrix composition, γ the specific interfacial energy of the particle/matrix boundary, V_P the molar volume of the particle, R_g the universal gas constant and R the particle radius. Considering the effect of the curvature of the particle, the supersaturation parameter of the cylindrical edges (k_t) should be expressed as [10, 19]

$$k_t = 2\frac{\left(C_I(\infty)\exp\left(\frac{2\gamma V_P}{R_g T}\frac{1}{S_0 - \lambda_p\sqrt{Dt}}\right) - C_M\right)}{\left(C_P - C_I(\infty)\exp\left(\frac{2\gamma V_P}{R_g T}\frac{1}{S_0 - \lambda_p\sqrt{Dt}}\right)\right)} \quad (15)$$

The dissolution rate from the cylindrical edges of the particles is related to the thermodynamics and kinetics of dissolution and also a geometrical problem that restricts the dissolution rate from the cylindrical edges. Assuming the cross section of the cylindrical edges in two dimensions to be a half-circle, the diameter of the cross section of the cylindrical edge of the particle should be equal to the thickness of the particle as a geometrically necessary condition (GNC) during dissolution. This geometrically necessary condition is schematically shown in Fig. 4. The radius of the cross section of the cylindrical edge during dissolution is restricted by the thickness of the particle and cannot decrease more than that even if the thermodynamic and the kinetics of dissolution would allow.

By applying the GNC, the cylindrical edges of the particles are not allowed to dissolve faster or more slowly than the planar surfaces. It should however be noted that the dissolution from the cylindrical edges and the planar surfaces has been modeled in different mathematical systems. In every specific time step, the dissolution from the cylindrical edge is independent of that from the planar surface. At the end of each time step, the cylindrical edge diameter is artificially assigned to be equal to the particle width. If the dissolution rate from the cylindrical edge is faster than that from the

surface, in a single time step, it will result in a larger decrease in the length of the particle, although the diameter should be always equal to the particle width. In this way, the increase in the concentration due to the curvature results in a higher dissolution rate of the cylindrical edges than that from the planar surfaces and therefore, the length decreases faster than the width. Due to the presence of the GNC, a boundary condition, presented in Eq. (16), is added to the system. This is necessary to be able to solve Eq. (12) with the conditions presented in Eq. (13) and (14).

$$C\left(r = S_0, t_h\right) = C_{\mathrm{Ih}} \qquad 0 < t < \infty \tag{16}$$

where C_{Ih} is the concentration at the particle matrix interface at the time the width of the particle has reached half of its initial value. It can be obtained by replacing R with $S_0/2$ in Eq. (14). There is a particular solution for the problem presented in Eq. (12) as [35]

$$C\left(r,t\right) = C_{\mathrm{M}} + \left(C_{Ih} - C_{\mathrm{M}}\right)\frac{t_h}{t}\frac{\exp\left(-\dfrac{r^2}{4Dt}\right)}{\exp\left(-\dfrac{{S_0}^2}{16Dt_h}\right)} \tag{17}$$

Eq. (3) can also be re-written in the case of a cylindrical particle,

$$\left(C_{\mathrm{P}} - C_{\mathrm{It}}\right)\frac{dR}{dt} = D\left(\frac{\partial C}{\partial r}\right) \qquad r = R \tag{18}$$

where C_{P} is a constant independent of r and t. Having obtained $C(r,t)$ and thus $\left(\dfrac{\partial C}{\partial r}\right)$ from Eq. (17), dR/dt may be obtained from Eq. (18) as

$$\frac{dR}{dt} = -\frac{R\left(C_{Ih} - C_{\mathrm{M}}\right)}{2\left(C_{\mathrm{P}} - C_{\mathrm{It}}\right)}\left(\frac{t_h}{t^2}\right)\frac{\exp\left(-\dfrac{R^2}{4Dt}\right)}{\exp\left(-\dfrac{{S_0}^2}{16Dt_h}\right)} \tag{19}$$

As discussed above, the radius itself must be equal to one half of the width of the

particle, as a geometrically necessary condition. Therefore, S_0 should be inserted into Eq. (19) for R at the initial time step. Afterwards, R should be replaced by S, which yields that the rate of the decrease in the radius of the cylindrical edge is a function of the rate of the decrease in the width of the particle. In other words, the dissolution rate from the cylindrical edges is a function of the difference between the concentration in the particle and the matrix, the radius of the cylindrical edge (which changes the concentration at the particle/matrix interface) and the rate of the decrease in the width of the particle.

As mentioned earlier, the radius of the cylindrical edge of a particle should be equal to one half of the particle thickness. Therefore, the thickness of the particle during dissolution, shown in Eq. (4) should be inserted into Eqs. (14) and (19), as the instantaneous radius of the particle, which for eq. (19) yields;

$$\frac{dR}{dt} = -\frac{1}{2}\left(S_0 - \lambda_p\sqrt{Dt}\right)\frac{\left(C_{Ih} - C_M\right)}{\left(C_P - C_{It}\right)}\left(\frac{t_h}{t^2}\right)\frac{\exp\left(-\frac{\left(S_0 - \lambda_p\sqrt{Dt}\right)^2}{4Dt}\right)}{\exp\left(-\frac{{S_0}^2}{16Dt_h}\right)} \qquad (20)$$

In order to determine the effect of the dissolution from the cylindrical edges of the particles, the relationship presented in Eq. (20) should be integrated over the time of dissolution. The integration yields the decrease in the length of the particle, l, as

$$l = -\frac{1}{2}\int_0^t \left(S_0 - \lambda_p\sqrt{Dt}\right)\frac{\left(C_{Ih} - C_M\right)}{\left(C_P - C_{It}\right)}\left(\frac{t_h}{t^2}\right)\frac{\exp\left(-\frac{\left(S_0 - \lambda_p\sqrt{Dt}\right)^2}{4Dt}\right)}{\exp\left(-\frac{{S_0}^2}{16Dt_h}\right)}\,dt \qquad (21)$$

Eq. (21) can be used to calculate the decrease in the length of the particle and the dissolution rate from the cylindrical edges.

3. Experimental procedure

Cubic samples of 2 cm on each side were cut from the centre of a direct-chill (DC) cast AA7020 billet. The chemical composition of the alloy is shown in Table 1. Isothermal homogenization treatments were performed in a salt bath at temperatures of 390, 430, 470, 510 and 550 °C for 2, 4, 8, 16, 24 and 48 hours. Following the heat treatment, the samples were water quenched.

The samples were examined using a JEOL 6500 field emission gun-scanning electron microscope (FEG-SEM). An optimum operating voltage for resolving the particles was found to be 10 kV which ensured sufficient penetration depth of electrons. Energy dispersive X-ray analysis (EDX) was also performed with an analyzer attached to the FEG-SEM to determine the chemical compositions of the particles.

The FEG-SEM images of the particles after different homogenization treatments were quantitatively analyzed to determine the extent of the dissolution of the particles during homogenization whereby 20 particles were analyzed in each case. The thickness of the particles was measured and the average value was calculated. During homogenization at high temperatures, i.e. 510 and 550 °C, some of the particles were completely dissolved in the structure. The dissolved particles were also considered in the calculation with a null thickness. The average initial number density of the particles in 20 micrographs was counted to be 0.002 μm^{-2}. The average number density of the particles after homogenization was also counted employing the same method and, if it was less than the average initial number density which indicated the full dissolution of some of the particles, a zero thickness was assumed instead of the vanished ones.

A BRUKER-AXS D5005 diffractometer with Cu kα1 wavelength was used to identify the phases present in the as-cast and as-homogenized conditions. Quantitative XRD (QXRD) analysis was performed using the direct comparison method [37] to estimate the weight percent of the phases in the structure. The application of this

method required the weight percent of the phase of interest in the as-cast structure (i.e., the $Al_{17}(Fe_{3.2},Mn_{0.8})Si_2$ particles in the present case), as the baseline. To calculate the weight percent of the particles in the as-cast structure, their surface fraction was calculated using FEG-SEM together with EDX which is capable of distinguishing between $Al_{17}(Fe_{3.2},Mn_{0.8})Si_2$ and other particles and providing a trustworthy initial surface fraction of $Al_{17}(Fe_{3.2},Mn_{0.8})Si_2$ particles in the as-cast microstructure. The analysis was performed on 20 images at a magnification of 1000 and all the particles present in each image were analyzed. Assuming a uniform distribution of the particles in the structure, the surface fraction was approximated to be equal to the volume fraction. The volume fraction of the $Al_{17}(Fe_{3.2},Mn_{0.8})Si_2$ particles was converted to weight percent using the density of the $Al_{17}(Fe_{3.2},Mn_{0.8})Si_2$ particle (3709 kg/m^3 [38, 39]) and the density of AA7020 aluminum alloy (2780 kg/m^3 [40]). The only assumption made was the density of the other particles (a mixture of various phases) other than the $Al_{17}(Fe_{3.2},Mn_{0.8})Si_2$, being equal to the density of AA7020 aluminum alloy.

4. Model inputs

4.1. Characteristics of the $Al_{17}(Fe_{3.2},Mn_{0.8})Si_2$ particles

The thermodynamically stable chemical composition for Al-Fe-Mn-Si compounds may be presented by $Al_{16}(Fe,Mn)_4Si_3$ or $Al_{15}(Fe,Mn)_3Si_2$ [41]. The crystallography of intermetallic phases containing aluminum, silicon, iron and manganese implies that they should be considered as phases with muledgele sublattices [42]. Therefore, these compounds may be simply considered as a solution of the Al-Fe-Si particles and Mn or vice versa. In that case, their formation and stability at different conditions obey the thermodynamics of solutions. Since Fe and Mn can reside on the same sublattices [42], the Al-Fe-Mn-Si particles can be considered $Al_{16}(Fe_{(1-y)},Mn_y)_4Si_3$. From the role of the

RT((1-y)ln(1-y)+ylny) term in the Gibbs free energy of solutions [43], it can be stated that a compound with equal values of Fe and Mn has the lowest total free energy.

In the DC-cast AA7020 aluminum alloy, the amount of Fe is higher than Mn in the grain boundary regions. The larger amount of Fe may be attributed to the partitioning coefficients of Fe and Mn which result in severer microsegregation of Fe toward the grain boundaries and, therefore, a higher concentration of Fe in these regions [44]. Fe has a small solid solubility in aluminum alloys [41]. Therefore, the excess Fe rather than what is consumed in Al-Fe-Mn-Si particles, must form other intermetallic compounds. In this case, if y=0.5, in addition to the thermodynamically stable $Al_{16}(Fe_{(1-y)},Mn_y)_4Si_3$ phase, some separate Al-Fe-Si and Al-Fe particles are expected to form to consume the remaining insoluble Fe at the grain boundaries. However, as mentioned above, the solution formation results in a decrease in the Gibbs free energy of the system determined by the -RT((1-y)ln(1-y)+ylny) term. Therefore, in this system, the stable Al-Fe-Mn-Si particles dissolve some of the excess Fe and form the meta-stable $Al_{17}(Fe_{3.2},Mn_{0.8})Si_2$ particles and the remaining Fe corporate in the formation of other intermetallic compounds. The amount of the Fe dissolved in the stoichiometric $Al_{16}(Fe_{(1-y)},Mn_y)_4Si_3$ particles is so much that the total energy of the system is minimized by the formation of $Al_{17}(Fe_{3.2},Mn_{0.8})Si_2$, Al-Fe-Si and Al-Fe particles. The formation of Al-Fe-Si and Al-Fe particles at the grain boundary regions has been revealed in the previous investigations of the authors [4, 45]. The same may be valid for the replacement of Si atom with exceeding Al in the compound from the stoichiometric values.

Low and higher magnification secondary electron FEG-SEM images of the as-cast microstructure of the AA7020 aluminum alloy are shown in Fig. 5. The $Al_{17}(Fe_{3.2},Mn_{0.8})Si_2$ particles elongated along the grain boundaries can be clearly seen.

The perturbations on the surfaces of the particles are illustrated with arrows in Fig. 5 (b).

Image analysis indicated that the volume fraction of the $Al_{17}(Fe_{3.2},Mn_{0.8})Si_2$ particles was close to 7%. Therefore, it was possible to determine the identity of these phases using XRD [37]. The results, shown in Fig. 6, illustrate that only one phase could be detected using XRD analysis, which was $Al_{17}(Fe_{3.2},Mn_{0.8})Si_2$. Comparison of the XRD results with those from EDX, as given in Table 2, indicates a good agreement.

The initial number density of $Al_{17}(Fe_{3.2},Mn_{0.8})Si_2$ particles per unit surface is 0.002 μm^{-2} ($2*10^9$ m^{-2}) with an average length of 68 μm. The average initial thickness of the particles was determined to be 640 nm. The average initial number of perturbations on the surface was determined to be 0.025 μm^{-1} (25000 m^{-1}). To calculate this number, the perturbations were considered as the places where the thickness is less than half of the average thickness of the particles, i.e. <320 nm. The measurements were obtained by counting the perturbations on 50 particles. The average thickness of the perturbations in the initial structure was calculated to be 256 nm.

Fig. 7 shows a particle after homogenization at 550 °C for 8 hours, demonstrating the occurrence of thinning and discontinuation, as described earlier. The occurrence of discontinuities during dissolution of the AA7020 alloy was the main reason for including the TDFD mechanism in the dissolution model. From this figure, it is clear that the distance between discontinuities is proportional to the distance between the initial perturbations, indicating that the discontinuities occur as a geometrical issue.

The experimental observations of the shapes of the particles, presented in Fig. 8, show that the cylindrical edges of the particles may initially have rectangular, ellipsoidal, needle or circular cross sections (Fig. 8 (a)-(c)). However, as shown in Fig.

8 (d)-(f), during the dissolution, the cylindrical edges have circular cross section. Assume the initial shape of the cylindrical edges to be rectangular having two steep cylindrical edges at the cylindrical edges. According to the Gibbs-Thompson equation (Eq. (14)), a large concentration of the solute at the interface is resulted in which indeed increases the dissolution rate significantly. The steep cylindrical edges dissolve sooner and therefore a circular cylindrical edge will be produced. The same is valid for an ellipsoidal cross section. It should be noted that the transition period from rectangle or ellipse to circle has not been considered in the model.

4.2. The initial constants of the model

The general features of the dissolution of particles during homogenization have been described by several investigators [10-32]. It is generally accepted that the dissolution is a thermally activated process, dependent on the solubility limit and diffusion rate of the alloying elements constituting the compound [10-32], mainly the element that has the lowest solubility limit and diffusion rate. By comparing the thermodynamic data of the three major alloying elements in the $Al_{17}(Fe_{3.2},Mn_{0.8})Si_2$ particles at homogenization temperatures, it is clear that Mn has the lowest diffusion coefficient [33]. This indicates that the diffusion of Mn in the matrix is the controlling parameter of dissolution kinetics.

5. Model validation

5.1. Volume fraction of the particles

Previous investigations [4] showed that during homogenization at temperatures lower than 470 °C, spheroidization of $Al_{17}(Fe_{3.2},Mn_{0.8})Si_2$ particles occurred, which resulted in a decrease in the area fraction. This might lead to misleading values during the validation of the model against the experimental results. Therefore, the validation of

the model has been made using the results of homogenization treatment only at 470 °C and higher.

Fig. 9 illustrates a comparison between the model predictions of the volume fraction of the particles dissolved at different homogenization temperatures, with the experimental FEG-SEM and XRD results. It is clear that in both of the graphs a reasonable agreement between the model predictions and the experimental results has been achieved.

It can be seen that the data from the quantitative FEG-SEM analysis show a better agreement. This is because the model presented herein is a two-dimensional model which considers the cross section of the $Al_{17}(Fe_{3.2},Mn_{0.8})Si_2$ particle for estimating the dissolution. The same procedure was used to calculate the volume fraction and the thickness of the $Al_{17}(Fe_{3.2},Mn_{0.8})Si_2$ particles using quantitative FEG-SEM analysis. In other words, the cross section of the $Al_{17}(Fe_{3.2},Mn_{0.8})Si_2$ particle has been considered and the volume fraction of dissolved particles calculated. However, the QXRD analysis works with the bulk of the material which can be considered a three dimensional problem.

Another factor which may result in minor discrepancies between the predicted and measured values is that in an industrial aluminum alloy, due to the presence of a large variety of alloying elements and impurities, a lot of constituent particles and precipitates are present, but not considered in this work. Moreover, the dissolution of the mentioned particles is a strong function of temperature and time. Some of these particles have similar XRD peaks, which may overlap each other and consequently result in discrepancies between the experimental results and the model predictions. However, such a problem is not valid in the case of QSEM because for each specific particle, the EDX analysis was used to ensure that the particle was an $Al_{17}(Fe_{3.2},Mn_{0.8})Si_2$ particle.

The dissolution of the $Al_{17}(Fe_{3.2},Mn_{0.8})Si_2$ particles into the aluminum matrix is dependent largely on the dissolution temperature. This is likely to be due to the strong dependence of the diffusion coefficient, the solubility limit of the matrix for the dissolving elements and consequently the supersaturation parameter and the volume fraction of particles on temperature. With increasing temperature, these parameters all increase, which results in an increase in the dissolution rate.

5.2. Widths of the particles

Fig. 10 shows a comparison between the model predictions for the thickness of the particles during homogenization at 470, 510 and 550 °C and the experimentally measured values using FEG-SEM. A reasonable agreement between the experimental results and model predictions has been reached.

6. Model predictions

6.1. The supersaturation parameter at the initiation of dissolution

The variations of the concentrations of the elements in the matrix exert influences on the dissolution rate by changing the deriving force for dissolution. The effect of the changes in the concentrations of the elements in the matrix and at the particle/matrix interface is incorporated into the model by the supersaturation parameter (k). Since the concentrations of the elements at the particle/matrix interface are functions of the shape of the interface, two supersaturation parameters may be defined, i.e., (i) for the planar surfaces (k_p) and (ii) for the cylindrical edges of the particles (k_t). In the case of the planar surfaces, the supersaturation parameter is a function of the concentrations of the dissolving elements in the particle, in the matrix and at the particle/matrix interface. In the case of the cylindrical edges, however, the supersaturation parameter is dependent not only on these variables, but also on the radii of the cylindrical edges, since these

affect the concentrations of the dissolving elements at the particle/matrix interface. See Eq. (14).

Fig. 11 illustrates the k_p and k_t values of the particles at different temperatures as a function of the initial width of the particles. It can also be seen that although k_p does not change with the width of the particle, k_t is strongly dependent on the width of the particle. This is expected because for k_p none of the variables are the functions of the width of the particle but for k_t these are. Since an increase in the supersaturation parameter is consistent with an increase in the driving force for dissolution and thus the dissolution rate, it can be concluded that at a given chemical composition, the dissolution rate of the particles with a smaller width is faster than the one with a larger width. The effect of the initial width of the particles is more significant on k_t at smaller widths. Regardless of temperature, when the width of the particles reaches 30 nm, the supersaturation parameter increases sharply. This results in an increase in the dissolution rate of the particles. These observations of k_t agree with the findings of Aaron and Kotler [10] who noted that in the case of spherical particles (in two dimensions, the similar geometrical conditions for the cylindrical edges of the particles), the dissolution rate would increase only if the size of the particles was rather small [10].

The effect of the initial width on the supersaturation parameter indicates that the dissolution rate of a particle having a small width is faster than a larger one such that the overall dissolution rate is dependent on the width of the individual particles. To avoid the complexity of the model, the average values of the initial widths of the particles have been calculated and used. However, since the relationship between the supersaturation parameter and the width is not linear; i.e., k increases sharply as the width reaches a specific value, the discrepancies between the model predictions and the experimental results may be yielded.

6.2. The supersaturation parameter during dissolution

Fig. 12 shows a comparison between k_p and k_t at different temperatures as a function of the width fraction of the particles dissolved, presented by $1\text{-}S/S_0$. It is clear that at the start of the dissolution process, i.e, $1\text{-}S/S_0=0$, k_t and k_p are close to each other, although at any conditions (at the beginning and during dissolution) k_t is larger than k_p. However, the difference between the k_t and the k_p increases as the width of the particle decreases ($1\text{-}S/S_0$ increases toward 1).

K_p decreases during dissolution. This is expected based on the definition of the supersaturation parameter, Eq. (6) since the concentrations of the dissolving elements in the matrix (C_M) increase. However, k_t first decreases when the width of the particles decreases, which, as mentioned earlier, is due to the increases in the concentrations of the dissolving elements in the structure. Afterwards, k_t increases significantly to such an extent that it exceeds the initial k_t value at the beginning of the dissolution process. The reason for this behavior is that when the width of the particle (i.e., the radius of the cylindrical edge) reaches small values, the effect of the radius of the cylindrical edge on the increase of the concentrations of the dissolving elements, C_{It}, dominates the increases in the concentrations of the dissolving elements in the matrix, C_M.

The decreases in k_p and k_t with the initial decreases in the particle width indicate the reductions in the dissolution rate. This trend continues till the end of the process for the planar surfaces of the particles (k_p). However, k_t increases, which indicates that at the finishing stages of dissolution the role of the dissolution from the cylindrical edges becomes more prominent. Based on these findings, it can be concluded that at the initiation of the dissolution process due to the large surfaces of the planar surfaces of the particles relative to their cylindrical edges (68 μm to 320 nm), the effect of the cylindrical edges on the dissolution is insignificant. Therefore, at this stage, the

assumption of neglecting the effect of the cylindrical edges on the dissolution is reasonable. However, as dissolution proceeds, the ratio of the dissolution from the cylindrical edges to that from the planar surfaces increases sharply, because the radius of the cylindrical edges decreases. Aaron and Kotler [10] concluded that for spherical precipitates dissolving in an infinite matrix, as time increased, the volume for mass transfer increased, thereby speeding up the dissolution rate. This is in fact the conditions occurring at the cylindrical edges of the plate-like particles, where with the decrease in the thickness of the particles and consequently the radius of the cylindrical edges, the dissolution rate from the cylindrical edges intensifies. This is different from the planar case, because the volume for mass transport ahead of the moving interface is always constant. In this case, k can only decrease as the concentrations of the dissolving elements in the matrix increase.

6.3. Interface position and interface movement rate

6.3.1. The effect of dissolution time and temperature

The dissolution of the particles occurs with the rejection of the constituting elements from the particles into the matrix, forcing the interface between the particle and matrix to move towards the particle center. Therefore, a study on the position of the interface and its movement rate is of importance to understand the extent of dissolution and the variations in the dissolution rate.

Fig. 13 shows the interface position of the planar surfaces and the cylindrical edges of the particle with respect to dissolution temperature, respectively. In this figure, the ratio of the instantaneous half width and half length of the particle (S and L) to the initial values (S_0 and L_0) is shown as a function of dissolution time. It is clear that the ratio decreases as the dissolution time increases. Both of the graphs show the same trend. The decrease in this ratio is due to the dissolution which forces the boundary to

move toward the particle center. It can be seen that the steep movement of the interface occurs at the beginning of the dissolution process (0-8 hours). To ascertain this, the interface movement rates for the planar surfaces and the cylindrical edges were calculated and presented in Fig. 14. It is clear that the interface movement rate from the cylindrical edges (v_t) is larger than that from the planar surfaces (v_p). The interface movement rate is directly related to the dissolution rate of the particle. It indicates that the dissolution rate from the cylindrical edges is higher than that from the planar surfaces.

Readey and Cooper [46] explained the differences between the dissolution kinetics of circular and planar particles from a physical point of view. The same explanations may be applied to account for the differences in dissolution rate between the cylindrical edges and planar surfaces of $Al_{17}(Fe_{3.2},Mn_{0.8})Si_2$ particles. According to Readey and Cooper [46], the main difference between the planar and circular geometries is that the area available for the transport of the diffusing elements increases along the radial distance from the center of a circle, but not from a planar interface. The dissolution rate of a circular surface initially decreases, followed by an increase with time as a consequence of the following two competing effects: the increase in the concentrations of the dissolving elements in the matrix which decreases the dissolution rate and the increase in the interfacial area of the sphere with decreasing size of the solute source relative to the surrounding area of the diffusion zone, which provides larger space for surface flux for the spherical particles. This is consistent with the observations of the trend of the k_t curves presented in Fig. 12, which shows that k_t initially decreases and then increases during dissolution. According to Readey and Cooper [46], the dissolution rate from the planar surfaces of the particle should decrease due to the increases in the concentrations of the dissolving elements in the matrix. This is valid for the planar

surfaces as shown in Fig. 14 (a). However, the dissolution rate from the cylindrical edges should first decrease and then increase when the cylindrical edges are small enough. As shown in Fig. 14 (b), this does not occur, which is because of the introduction of the geometrically necessary condition into the model that restricts the decrease in the size of the cylindrical edge.

The ratio of the interface movement rate of the cylindrical edges to that of the planar surfaces (v_t / v_p) is illustrated in Fig. 15. It is clear that the ratio increases as the dissolution temperature increases. In addition, with increasing dissolution time the ratio increases. Both of these two effects are due to the decrease in the width of the particles; i.e, the radius of the cylindrical edges. The increase in the ratio indicating that the interface movement rate of the cylindrical edges is higher than that of the planar surfaces is consistent with the findings of Readey and Cooper [46] who found that the dissolution rate of the spherical precipitates increased at the final stages of dissolution.

As discussed earlier, the reason for the decreasing trend of the dissolution rate from the planar surfaces is due to the increase in the concentrations of the dissolving elements in the matrix which decreases the driving force for dissolution. However, at the cylindrical edges, there are four effective parameters: (i) the increase in the matrix concentration, (ii) the geometrically necessary condition, (iii) the increase in the concentrations of the dissolving elements at the particle/matrix interface due to the effect of the interface curvature and (iv) the increase in the interfacial area of the cylindrical edge with decreasing size of the solute source relative to the surrounding area of the diffusion zone which provides larger space for surface flux for the circular particle. It should be noted that the first two parameters decrease the interface movement rate, while the last two increase the interface movement rate.

The concentration gradient at the interface of the cylindrical edge initially

decreases with time due to increased solute concentrations in the matrix near the interface. This influence is of major importance at short times when the gradient decreases sharply from its original semi-infinite value. As the cylindrical edge becomes smaller, the interface movement rate keeps increasing, because the interfacial area of the cylindrical edge decreases markedly. This also results in decreasing size of the solute source relative to the area of the surrounding diffusion zone. The total flux at the cylindrical edge surface is affected by the area available for diffusion throughout the diffusion zone and the rate of cylindrical edge shrinkage is equal to the surface flux divided by the cylindrical edge surface area. Moreover, with decreasing radii of the cylindrical edges, the concentrations of the dissolving elements at the particle/matrix interface increase, leading to an increase in the concentration gradient, which in turn increases the interface movement rate. However, the geometrically necessary condition also prohibits the cylindrical edges to decrease in size significantly. The continuous decrease in the interface movement rate indicates that the effective parameters on the increase in the interface movement rate do not dominate the influence of increased solute concentrations and the physical restriction from the geometrically necessary condition. The increase in the ratio of the interface movement rate from the cylindrical edges to that from the planar surfaces is evident, which indicates the effectiveness of the curvature of the cylindrical edge and the increase in the interfacial area of the cylindrical edge in the enhancement of dissolution rate from the cylindrical edges.

6.3.2. The dependence of the interface movement rate on the width of the particles

Fig. 16 shows the effect of the width fraction of the particles dissolved (presented by $1\text{-}S/S_0$) on the interface movement rate of the planar surfaces and the cylindrical edges, in logarithmic scale. The interface movement rates of the planar surfaces and the cylindrical edges increase with increasing dissolution temperature. During dissolution,

the highest interface movement rate occurs at the beginning of the process and the interface movement rates decrease steeply afterwards.

Fig. 17 shows the dependence of the ratio of the dissolution rate from the cylindrical edges to that from the planar surfaces as a function of particle width. It can be seen that the ratio is lower at higher temperatures. This indicates that the only reason for the increase in the ratio at higher temperatures, presented in Fig. 15, is the decrease in the width of the particles due to faster dissolution of the planar surfaces at higher temperatures. This can be confirmed by examining Eq. (14) that illustrates the effective parameters on C_{It}. It can be seen that with increasing dissolution temperature, C_{It} decreases. Therefore, the only role of temperature that intensifies the fraction of dissolution from the cylindrical edges over the planar surfaces is the effect of temperature on the decrease in the width of the particles. This provides a convenient situation for faster dissolution from the cylindrical edges due to the presence of the geometrically necessary condition and also by increasing C_{It} as a result of the decreasing radius of the cylindrical edge.

6.3.3. The effect of the geometrically necessary condition on the interface movement rate of the cylindrical edges

The introduction of the geometrically necessary condition into the model restricts the cylindrical edges from decreasing in diameter more than that allowed by the width of the particle. The reason that the interface movement rate of the cylindrical edges does not increase after the decrease at the beginning of dissolution has been attributed to the presence of the geometrically necessary condition. Fig. 18 shows the effect of the geometrically necessary condition on the interface movement rate of the cylindrical edges. It is clear that, considering that effect, the interface movement rate decreases. In addition, the increase in the interface movement rate at the end of the dissolution

process, i.e., 1-S/S_0 close to 1, is clear. This is expected according to the findings of Readey and Cooper [46] and also the observations of k_t in Fig. 12. From Fig. 18, it can also be concluded that neglecting the effect of the geometrically necessary condition on the interface movement rate can cause a significant error in the model predictions.

6.4. The ratio of dissolution from the cylindrical edges to that from the planar surfaces (the effect of discontinuities)

Fig. 19 presents the ratio of the volume fraction of the particles dissolved from the cylindrical edges to that dissolved from the planar surfaces (f_t / f_p), with and without including the effect of the occurrence of the discontinuities. The small value of the ratio is because the planar surfaces are much larger than the cylindrical edges and therefore, the amount of dissolution from the planar surfaces is much larger than the cylindrical edges. The reason for the increase in the ratio has been discussed earlier. It is clear from Fig. 19 that the fraction of the dissolution rate from the cylindrical edges becomes larger at higher temperatures and longer times when the radii of the cylindrical edges become smaller.

The time required for the discontinuities to occur is also shown in Fig. 19. It can be seen that due to the occurrence of the discontinuities, the ratio increases sharply. Comparing the effect of the occurrence of the discontinuities on the ratio at different temperatures to the conditions without the discontinuities shows that regardless of the dissolution temperature, by the occurrence of discontinuities, the ratio of the dissolution from the cylindrical edges to that from the planar surfaces increases. The ratio is the same when the discontinuities do not occur and afterwards, a sudden increase is observed due to the occurrence of the discontinuities which is coincident with the formation of new cylindrical edges, leading to an increase in the number density of the cylindrical edges. This results in a large increase in the ratio of the dissolution from the

cylindrical edges to that from the planar surfaces.

7. Conclusions

The TDFD dissolution mechanism proposed for the $Al_{17}(Fe_{3.2},Mn_{0.8})Si_2$ particles in the AA7020 aluminum alloy has been mathematically expressed using a diffusion limited dissolution model, taking the dissolution from the planar surfaces and the cylindrical edges of the particles into consideration. The occurrence of the discontinuities which has not been reported previously, has been incorporated into the model which intensifies the dissolution rate by increasing the number density of the cylindrical edges. The dissolution rate from the planar surfaces has been considered dependent on the differences between the concentrations in the particle, in the matrix and at the particle/matrix interface. The dissolution rate from the cylindrical edges has been considered to be dependent on the concentrations of the elements in the matrix and the particle, radius of the cylindrical edge and also the dissolution rate from the planar surfaces. The later has been incorporated into the model applying a geometrically necessary condition. The changes in the concentration of the matrix have been considered in the model by calculating the average values of the dissolved elements in the matrix for the change in the concentration of the matrix in each time step. For a given initial volume fraction and thickness of the particles, this model is capable of predicting the volume fraction and the thickness of the $Al_{17}(Fe_{3.2},Mn_{0.8})Si_2$ particles during homogenization at different temperatures and times. The model predictions of the volume fraction of the $Al_{17}(Fe_{3.2},Mn_{0.8})Si_2$ particles and their thicknesses have been validated with experimental QSEM and QXRD results and a good agreement is found. Based on these results, the following conclusions have been drawn:

1- The dissolution of the $Al_{17}(Fe_{3.2},Mn_{0.8})Si_2$ particles into the aluminum matrix is dependent largely on the dissolution temperature. This is due to the strong

dependence of diffusion coefficient, the solubility limit of the dissolving elements in the matrix and consequently the supersaturation parameter (k). With increasing temperature, these parameters increase, which results in increases in dissolution rate.

2- Due to the large surfaces of the planar parts of the particles compared to their cylindrical edges, the fraction of the dissolution from the cylindrical edges is insignificant at the beginning of the dissolution process. Therefore, at the start of the process, the assumption of neglecting the effect of the cylindrical edges on the dissolution is reasonable. However, as the dissolution process continues the ratio of the dissolution from the cylindrical edges to that from the planar surfaces increases steeply. In addition, considering the TDFD dissolution mechanism, the number density of the cylindrical edges increases. Consequently including the effect of the dissolution from the cylindrical edges in the model is necessary.

3- The decreasing trend of the changes in the interface movement rate (dissolution rate) from planar surfaces is due to the increase in the concentrations of the dissolving elements in the matrix, which decreases the concentration gradients and therefore the driving force for dissolution. However, in the case of the cylindrical edges there are four effective parameters on the interface movement rate, namely (i) the decrease in the concentration gradient, (ii) the geometrically necessary condition, (iii) the increase in the concentrations of the dissolving elements at the particle/matrix interface due to the effect of the interface curvature and (iv) the increase in the interfacial area of the cylindrical edge with decreasing size of the solute source relative to the area of the surrounding diffusion zone.

4- At a given particle width, the ratio of the dissolution from the cylindrical edges to that from the planar surfaces is lower at higher temperatures. The only reason for the ratio of the dissolution from the cylindrical edges to that from the planar surfaces at

higher temperatures to increase is the lower width of the particles as a result of rapid dissolution of the planar surfaces but not due to the temperature effect. In other words, the only effect of the increase in temperature that increases the fraction of the dissolution from the cylindrical edges over the planar surfaces is the effect of temperature on the decrease in the width of the particle which provides a convenient situation from the geometrically necessary condition point of view and also by increasing C_{It} by decreasing the radius of the cylindrical edge.

5- At the beginning of the dissolution process, the ratio of the dissolution from the cylindrical edges to the planar surfaces is small. This ratio increases later on as a result of increases in the dissolution rate from the cylindrical edges due to the decrease in the radii of the cylindrical edges and by increasing the number density of the cylindrical edges. Without considering the occurrence of the discontinuities, the ratio of the volume fraction of the particles dissolved from the cylindrical edges to that from the planar surfaces increases due to the increases in the concentration gradient and the interfacial area of the cylindrical edges. With considering the discontinuities, however, this ratio increases almost two times, which is due to the increases in the number density of the cylindrical edges of the particles together with the other two mentioned effects.

Acknowledgements

This research was carried out under the project number MC 4.04203 in the framework of the Research Program of the Materials Innovation Institute M2i (www.m2i.nl), the former Netherlands Institute for Metals Research. The authors acknowledge Mr. C. Kwakernaak, Mr. R.W.A. Hendrikx, Mr. N.M. van der Pers and Mr. E.R. Peekstok for assistance in performing XRD experiments and providing access to SEM.

References

[1] T. Sheppard, *Extrusion of Aluminum Alloys*, Kluwer Academic Publishers, Dordrecht, 1999.

[2] A. Jackson, T. Sheppard, in Proceedings of the 6th International Aluminum Extrusion Technology Conference, Volume 1, 1996, p. 541-550.

[3] G.T. Hahn, A.R. Rosenfield, Metall. Trans. A 6 (1975) p.653.

[4] A.R. Eivani, H. Ahmed, J. Zhou, J. Duszczyk, Metal. Mater. Trans. A 40 (2009) p.717.

[5] D.S. Thompson, Metall. Trans. A 6 (1975) p.671.

[6] G.G. Garrett, J.F. Knott, Metall. Trans. A 9 (1978) p.1187.

[7] F.Y. Xie, T. Kraft, Y. Zuo, C.H. Moon, Y.A. Chang, Acta Mater. 47 (1999) p.489.

[8] J.S. Robinson, Mater. Sci. Technol. 19 (2003) p.1697.

[9] L.L. Rokhlin, T.V. Dobatkina, N.R. Bochvar, E.V. Lysova, J. Alloys Compd. 367 (2004) p.10.

[10] H.B. Aaron, G.R. Kotler, Metal. Trans. 2 (1971) p.393.

[11] M.J. Whelan, Metal. Sci. J. 3 (1969) p.95.

[12] F.V. Nolfi, P.G. Shewmon, J.S. Foster, Trans. Metal. Soc. AIME 245 (1969) p.1427.

[13] R.A. Tanzilli, R.W. Heckel, Trans. Metal. Soc. AIME 242 (1968) p.2313.

[14] U.H. Tundal, N. Ryum, Metal. Trans. A 23 (1992) p.433.

[15] U.H. Tundal, N. Ryum, Metal. Trans. A 23 (1992) p.445.

[16] F.J. Vermolen, C.J. Vuik, J. Comp. Appl. Math. 126 (2000) p.233.

[17] F.J. Vermolen, S.vd. Zwaag, Mater. Sci. Eng. A 220 (1996) p.140.

[18] N. Nojiri, M. Enomoto, Scr. Metal. Mater. 32(5) (1995) p.787.

[19] H.B. Aaron, D. Fainstein, G.R. Kotler, J. Appl. Phys. 41 (1970) p.4404.

[20] M. Sinder, J. Pelleg, Metal. Mater. Trans. A 31 (2000) p.1525.

[21] F.J. Vermolen, C. Vuik, S.vd. Zwaag, Mater. Sci. Eng. A 328 (2002) p.14.

[22] H. Chen, J.E. Morral, Acta Mater 47(4) (1999) p.1175.

[23] Q. Chen, N. Ma, K. Wu, Y. Wang, Scr. Mater. 50 (2004) p.471.

[24] S. Chen, M.S. Vossenberg, F.J. Vermolen, J.vd. Langkruis, Mater. Sci. Eng. A 272 (1999) p.205.

[25] P. Hewitt, E.P. Butler, Acta Metall. 34(7) (1986) p.1163.

[26] N. Matan, H.M.A. Winand, P. Carter, M. Karunartne, P.D. Bogdanoff, R.C. Reed, Acta Mater. 46(13) (1998) p.4587.

[27] G. Segal, K. Vuik, F.J. Vermolen, J. Comp. Physics 141 (1998) p.1.

[28] F.J. Vermolen, P.vd. Mourik, S.vd. Zwaag, Mater. Sci. Tech. 13 (1997) p.308.

[29] F.J. Vermolen, C. Vuik, S.vd. Zwaag, Mater. Sci. Eng. A 347 (2003) p.265.

[30] F.J. Vermolen, C.J. Vuik, Comp. Applied Math. 93 (1998) p.123.

[31] Vermolen FJ, Vuik C, Zwaag Svd. Mathematical Models for Particle Dissolution in Metallic Alloys, in Reports of the Department of Applied Mathematics. 2002, TU-Delft.

[32] T.L. Durbin, *Modeling dissolution in aluminum alloys*, Mechanical Engineering Department, Georgia Institute of Technology, 2005.

[33] Y. Du, Y.A. Chang, B. Huang, W. Gong, J. Jin, H. Xu, Z. Yuan, Y. Liu, Y. He, F.Y. Xie, Mater. Sci. Eng. A 363(1-2) (2003) p.140.

[34] D.A. Porter, K.E. Easterling, *Phase Transformation in Metals and Alloys*, VNR International, London, 1981.

[35] A.D. Polyanin, *Handbook of Linear Partial Differential Equations for Engineers and Scientists*, Chapman & Hall/CRC Press, Boca Raton, 2002.

[36] M. Hillert (ed.), *Lectures on the theory of phase transformations,* Warrendale, TMS, 2000.

[37] B.D. Cullity, S.R. Stock, S. Stock, *Elements of X-Ray Diffraction*, 3 rd ed., Addison Wesley publishing company, California, 2001.

[38] International Center for Diffraction Data (ICDD), (2005) Powder Diffraction File Number (PDF no.) 01-071-4015.

[39] M. Cooper, Acta Crystallogr 23 (1967) p.1106.

[40] ASM Handbook: Volume 2: ASM International; 10 ed., 1992.

[41] N.A. Belov, D.G. Eskin, A.A. Aksenov, *Multicomponent Phase Diagrams: Applications for Commercial Aluminum Alloys*, Elsevier Science, New York, 2005.

[42] R.W. Cahn, P. Haasen, *Physical Metallurgy*, North Holland, Amsterdam, 1996.

[43] D. Gaskell, *Introduction to the Thermodynamics of Materials*, Taylor & Francis Co., New York, 2003.

[44] R. Nadella, D.G. Eskin, Q. Du, L. Katgerman, Prog. Mater. Sci. 53(3) (2008) p.421.

[45] A.R. Eivani, H. Ahmed, J. Zhou, J. Duszczyk, Proc 11th Int Conf aluminum alloys 2008 Aachen, Germany, pp. 993-999.

[46] D.W. Readey, A.R. Cooper, Chem. Eng. Sci. 21 (1966) p.917.

Figure	Caption
Figure 1	The schematic view of the dissolution of an $Al_{17}(Fe_{3.2},Mn_{0.8})Si_2$ particle in AA7020 through the TDFD mechanism, (a) the initial particle with perturbations, (b) through (d) thinning of the particle, (e) and (f) occurrence of the discontinuities, leading to an increase in the number density of the cylindrical edges.
Figure 2	The dissolution of an $Al_{17}(Fe_{3.2},Mn_{0.8})Si_2$ particle from its planar surfaces and cylindrical edges into the grain interior.
Figure 3	The schematic view of an $Al_{17}(Fe_{3.2},Mn_{0.8})Si_2$ particle with initial perturbations. The dissolution from the planar surfaces of the $Al_{17}(Fe_{3.2},Mn_{0.8})Si_2$ particle can be modeled, considering a one-dimensional model for the dissolution of a plate-like particle from its surfaces. The dissolution from the cylindrical edges can be modeled, considering the dissolution from the surface of a half cross section of a two-dimensional cylinder.
Figure 4	Schematic view of the geometrically necessary condition (GNC) which determines the radius of the cylindrical edge of the $Al_{17}(Fe_{3.2},Mn_{0.8})Si_2$ particle during dissolution, a) the geometrically permissible condition, b) and c) the geometrically impermissible conditions.
Figure 5	Low (a) and higher (b) magnification FEG-SEM micrographs showing the $Al_{17}(Fe_{3.2},Mn_{0.8})Si_2$ particles in the as-cast

	microstructure.
Figure 6	X-ray diffraction pattern of the as-cast material showing the presence of the $Al_{17}(Fe_{3.2},Mn_{0.8})Si_2$ particles.
Figure 7	An $Al_{17}(Fe_{3.2},Mn_{0.8})Si_2$ particle after homogenization at 550 °C for 8 hours, showing the thinning and discontinuation.
Figure 8	The shape of the cylindrical edges of the $Al_{17}(Fe_{3.2},Mn_{0.8})Si_2$ particles, (a) through (c) in the initial structure, (d) through (f) after homogenization at 550 °C for 8 hours. In (d) through (f), a circle has been drawn on the cylindrical edges of the particles, showing the perfectness of the circular cross section of the cylindrical edges.
Figure 9	Comparison of the model predictions of the volume fraction of the particles dissolved at different temperatures with the results obtained using (a) quantitative FEG-SEM (QSEM) and (b) quantitative XRD analysis (QXRD).
Figure 10	Comparison between the model predictions of the thickness of the particles dissolved during homogenization at different temperatures, and the experimental measurements using FEG-SEM.
Figure 11	A comparison between the supersaturation parameter of the planar surfaces (k_p) and the cylindrical edges (k_t) of the particles at different temperatures as a function of the initial width of the particles.
Figure 12	A comparison between the supersaturation parameter of the planar surfaces (k_p) and the cylindrical edges (k_t) of the particles at different temperatures as a function of the width fraction of the particles

	dissolved (1-S/S_0).
Figure 13	(a) The interface position of the planar surface of the particle and (b) The interface position of the cylindrical edges of the particle.
Figure 14	(a) The interface movement rate of the planar surfaces of the particles (v_p) and (b) The interface movement rate of the cylindrical edges of the particles (v_t).
Figure 15	The ratio of the interface movement rate from the cylindrical edges to that from the planar surfaces (v_p / v_t).
Figure 16	The dependence of the interface movement rate of the (a) planar surfaces (v_p) and (b) the cylindrical edges (v_t) on the width fraction of the particles dissolved (1-S/S_0) at different temperatures. The *y* axis is shown in a logarithmic scale.
Figure 17	The ratio of the interface movement rate from the cylindrical edges to that from the planar surfaces (v_p / v_t) as a function of the width fraction of the particles dissolved (1-S/S_0) at various homogenization temperatures.
Figure 18	The effect of the geometrically necessary condition (GNC) on the interface movement rate of the cylindrical edges (v_t).
Figure 19	The ratio of the volume fraction of the particles dissolved from the cylindrical edges to that from the planar surfaces (f_p / f_t), with the effect of the occurrence of the discontinuities taken into consideration. The times of occurrence of discontinuities have been also shown on the figure with vertical lines.

Table	Caption
Table 1	Chemical composition of the alloy used in this study
Table 2	Measured mean compositions (wt %) of the grain boundary constitutive particles in the as-cast material together with the calculated chemical compositions of the suggested phase identity based on the XRD analysis.

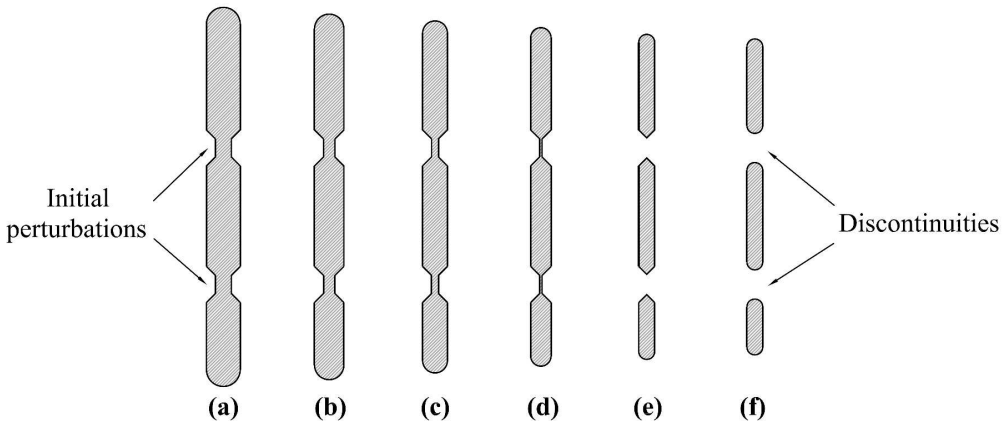

The schematic view of the dissolution of an Al17(Fe3.2,Mn0.8)Si2 particle in AA7020 through the TDFD mechanism, (a) the initial particle with perturbations, (b) through (d) thinning of the particle, (e) and (f) occurrence of the discontinuities, leading to an increase in the number density of the cylindrical edges.
955x403mm (96 x 96 DPI)

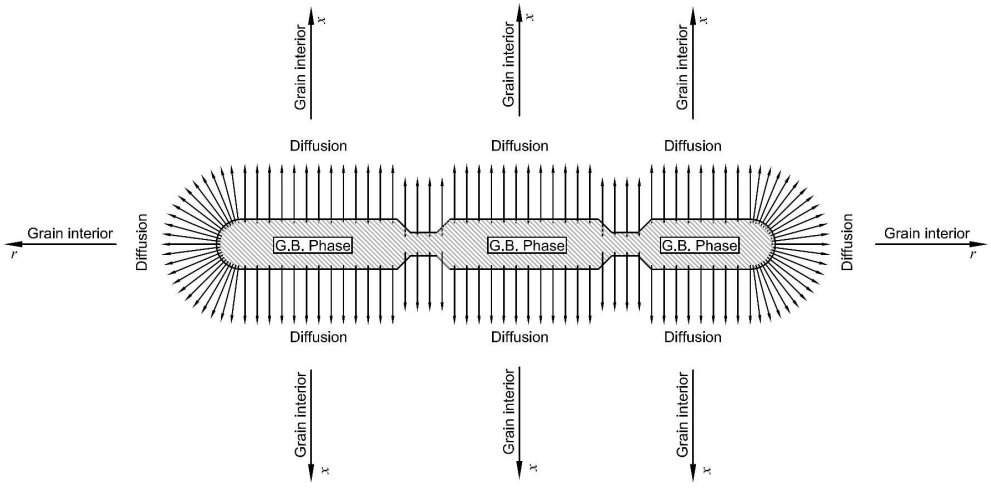

The dissolution of an Al17(Fe3.2,Mn0.8)Si2 particle from its planar surfaces and cylindrical edges into the grain interior.
954x464mm (96 x 96 DPI)

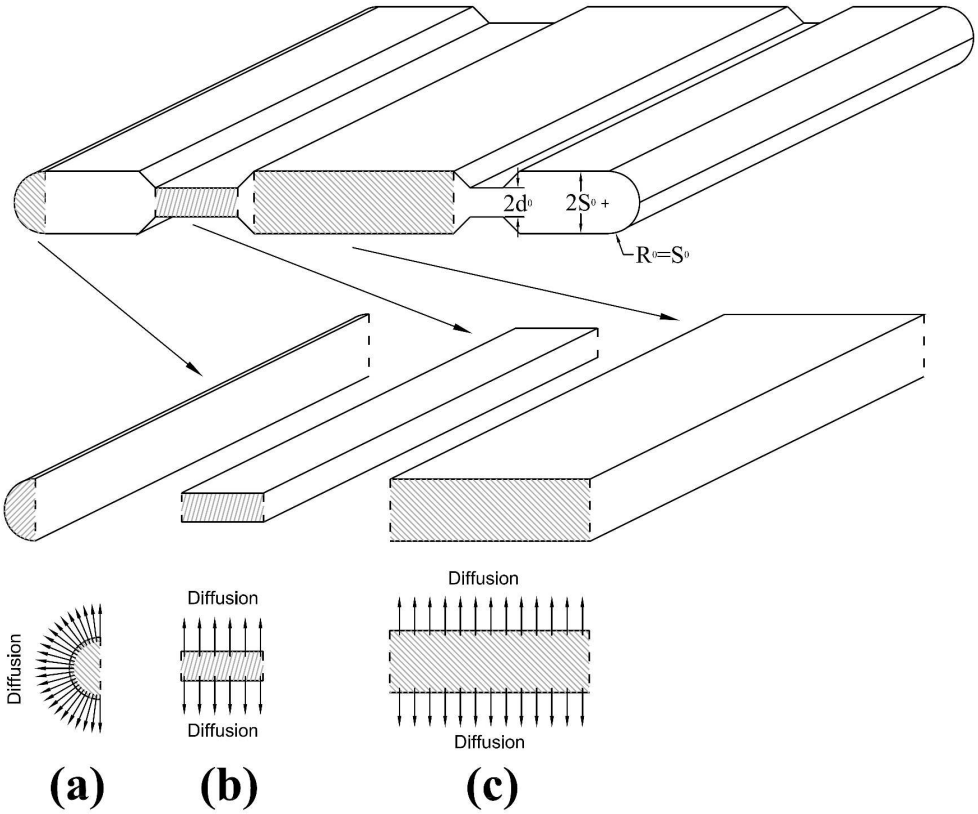

The schematic view of an Al17(Fe3.2,Mn0.8)Si2 particle with initial perturbations. The dissolution from the planar surfaces of the Al17(Fe3.2,Mn0.8)Si2 particle can be modeled, considering a one-dimensional model for the dissolution of a plate-like particle from its surfaces. The dissolution from the cylindrical edges can be modeled, considering the dissolution from the surface of a half cross section of a two-dimensional cylinder.
942x784mm (96 x 96 DPI)

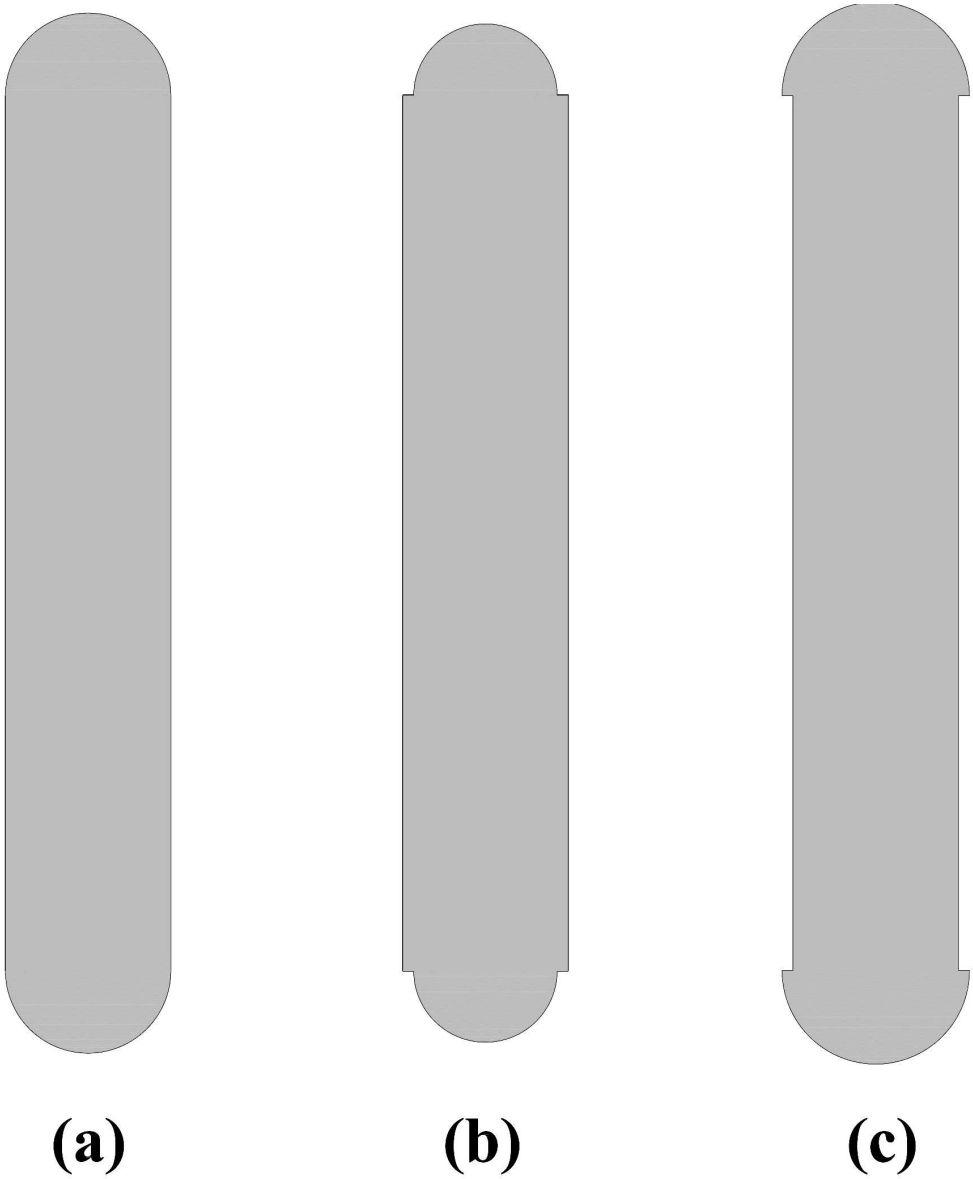

Schematic view of the geometrically necessary condition (GNC) which determines the radius of the cylindrical edge of the Al17(Fe3.2,Mn0.8)Si2 particle during dissolution, a) the geometrically permissible condition, b) and c) the geometrically impermissible conditions.
935x1109mm (96 x 96 DPI)

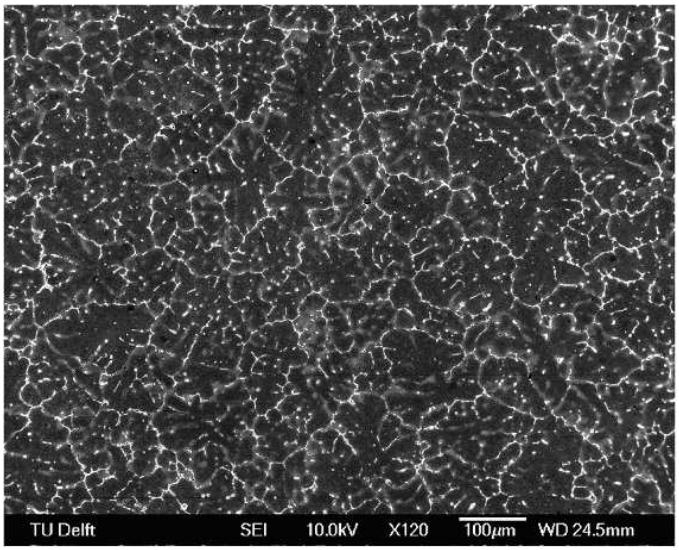

(a)

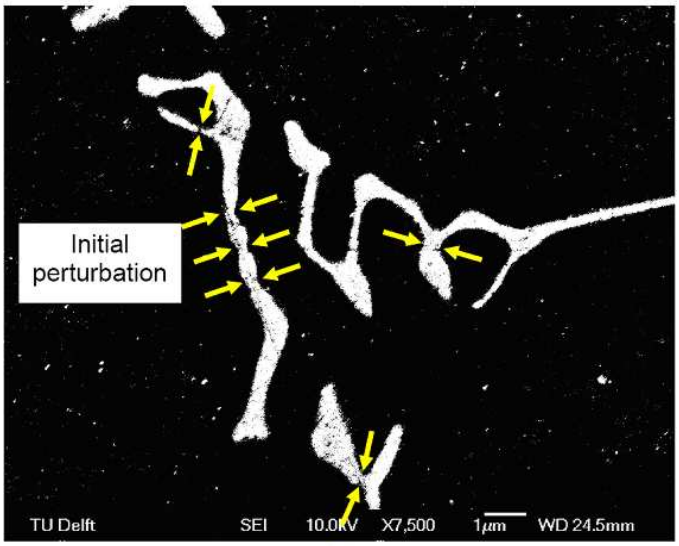

(b)

Low (a) and higher (b) magnification FEG-SEM micrographs showing the Al17(Fe3.2,Mn0.8)Si2 particles in the as-cast microstructure.
150x266mm (96 x 96 DPI)

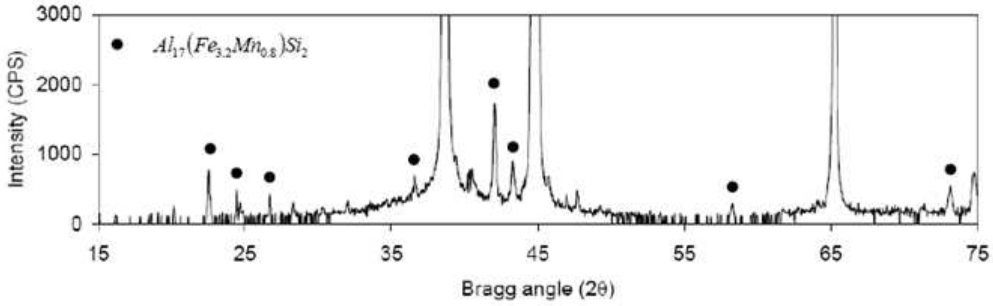

X-ray diffraction pattern of the as-cast material showing the presence of the Al17(Fe3.2,Mn0.8)Si2 particles.
176x66mm (96 x 96 DPI)

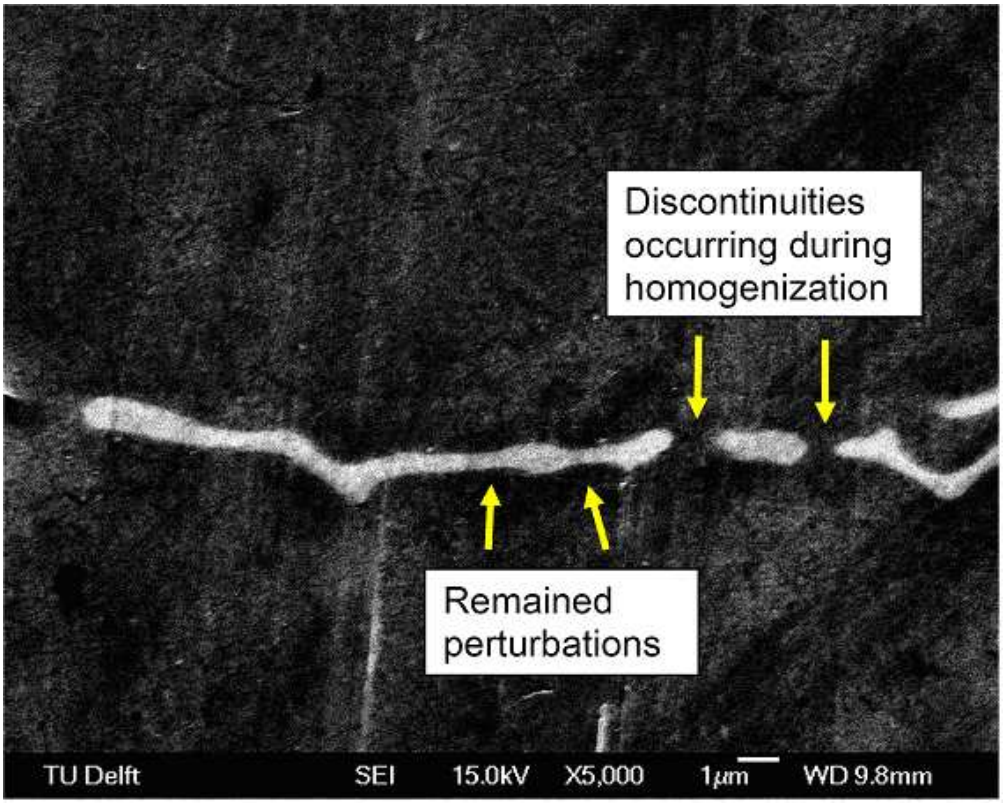

An Al17(Fe3.2,Mn0.8)Si2 particle after homogenization at 550 °C for 8 hours, showing the thinning and discontinuation.
150x120mm (96 x 96 DPI)

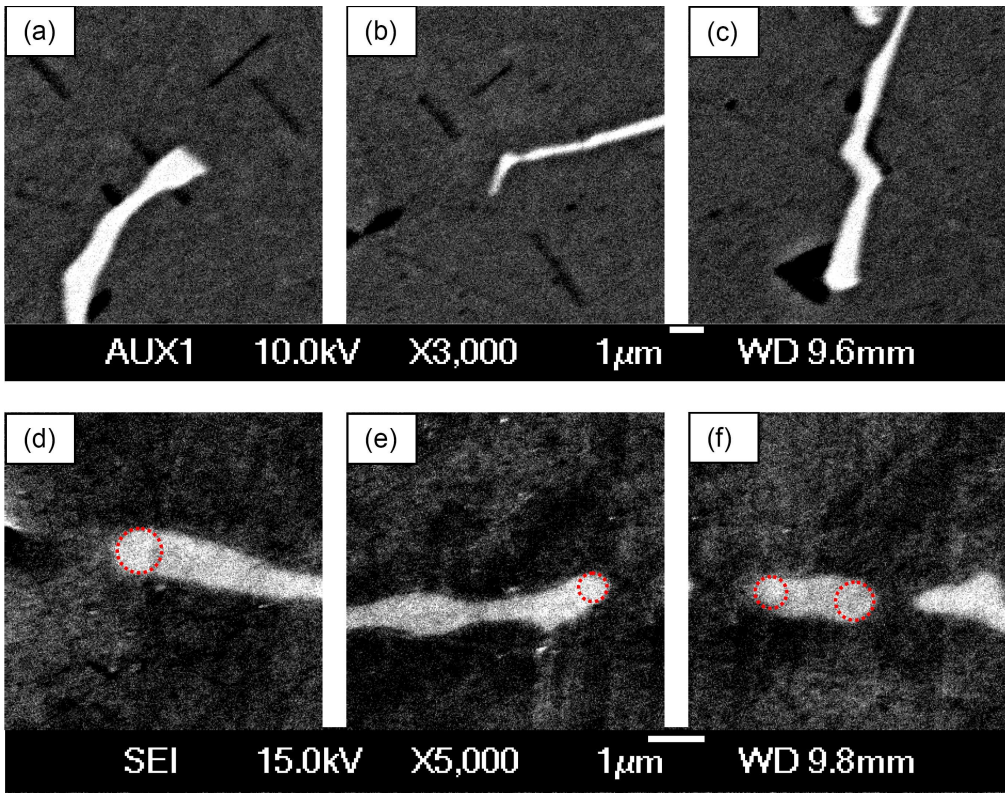

The shape of the cylindrical edges of the Al17(Fe3.2,Mn0.8)Si2 particles, (a) through (c) in the initial structure, (d) through (f) after homogenization at 550 °C for 8 hours. In (d) through (f), a circle has been drawn on the cylindrical edges of the particles, showing the perfectness of the circular cross section of the cylindrical edges.
723x569mm (96 x 96 DPI)

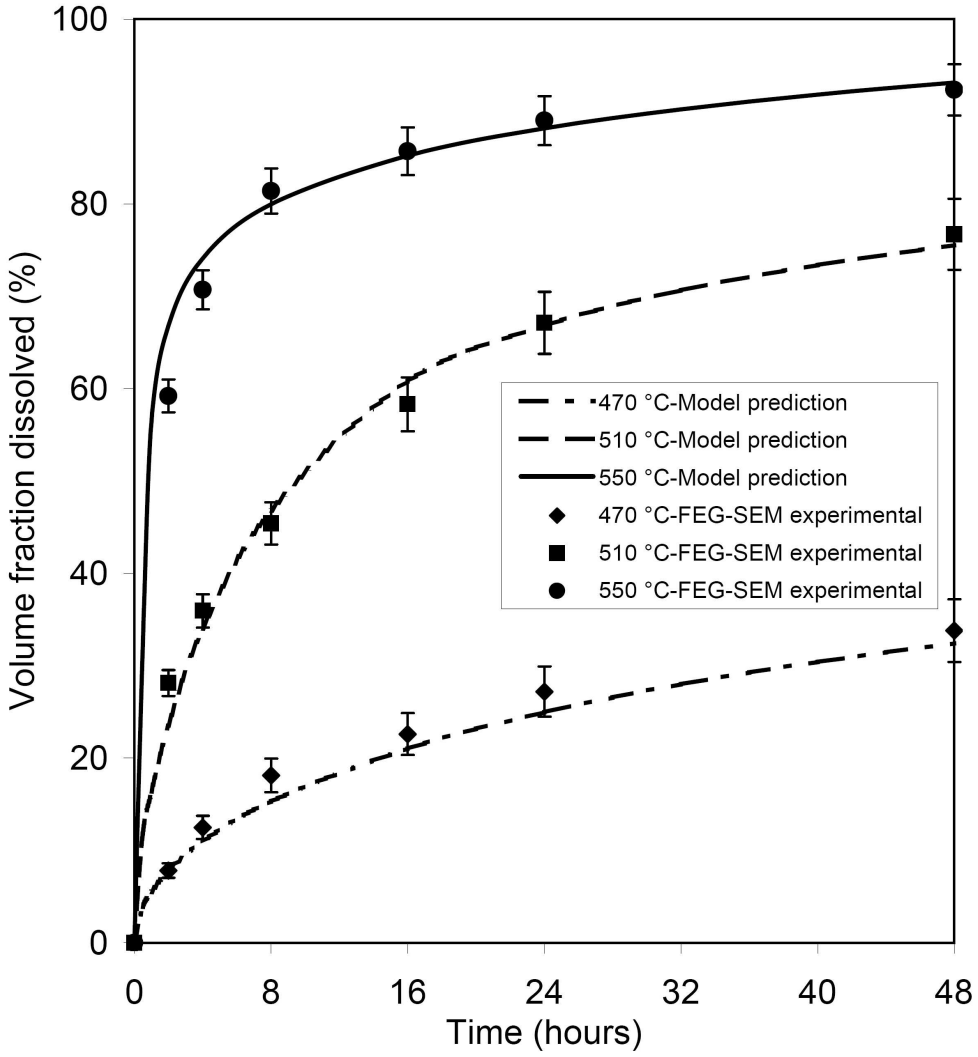

Comparison of the model predictions of the volume fraction of the particles dissolved at different temperatures with the results obtained using (a) quantitative FEG-SEM (QSEM) and (b) quantitative XRD analysis (QXRD).
644x692mm (96 x 96 DPI)

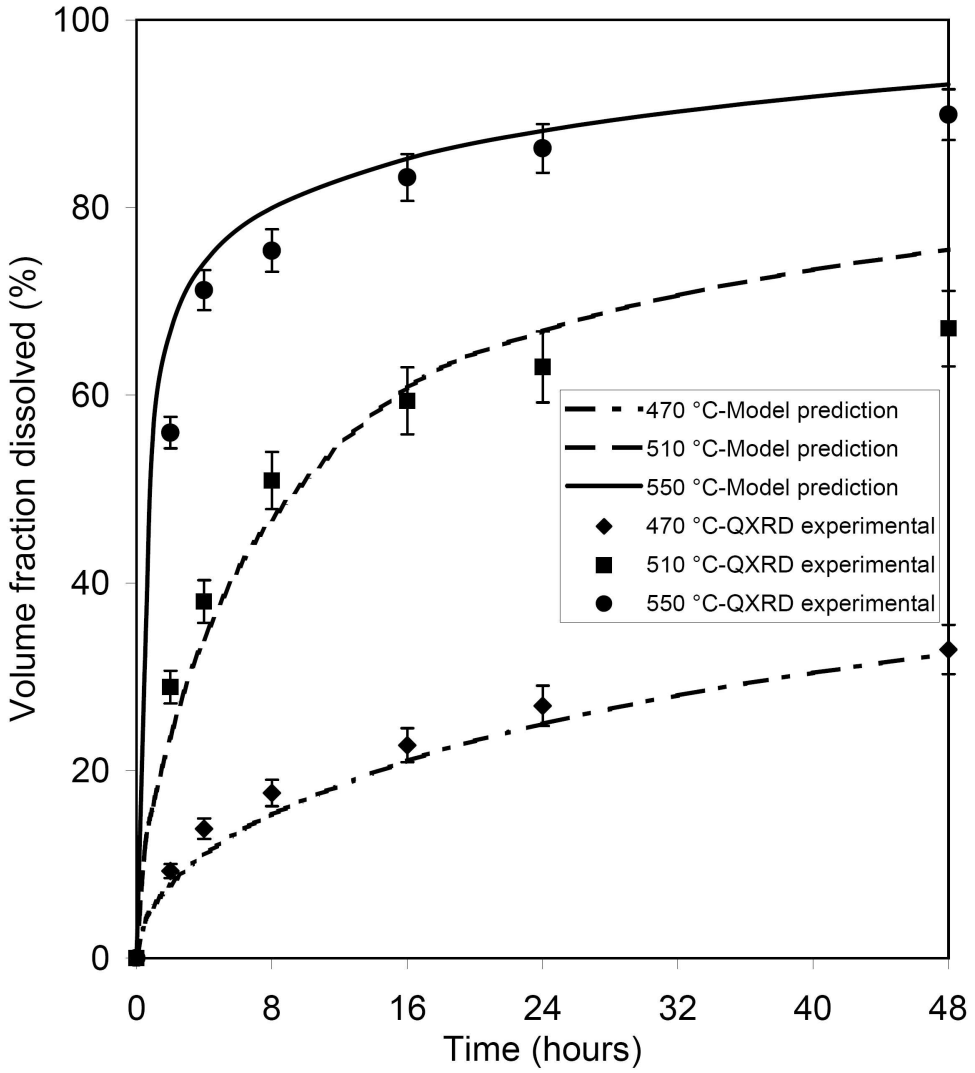

Comparison of the model predictions of the volume fraction of the particles dissolved at different temperatures with the results obtained using (a) quantitative FEG-SEM (QSEM) and (b) quantitative XRD analysis (QXRD).
635x692mm (96 x 96 DPI)

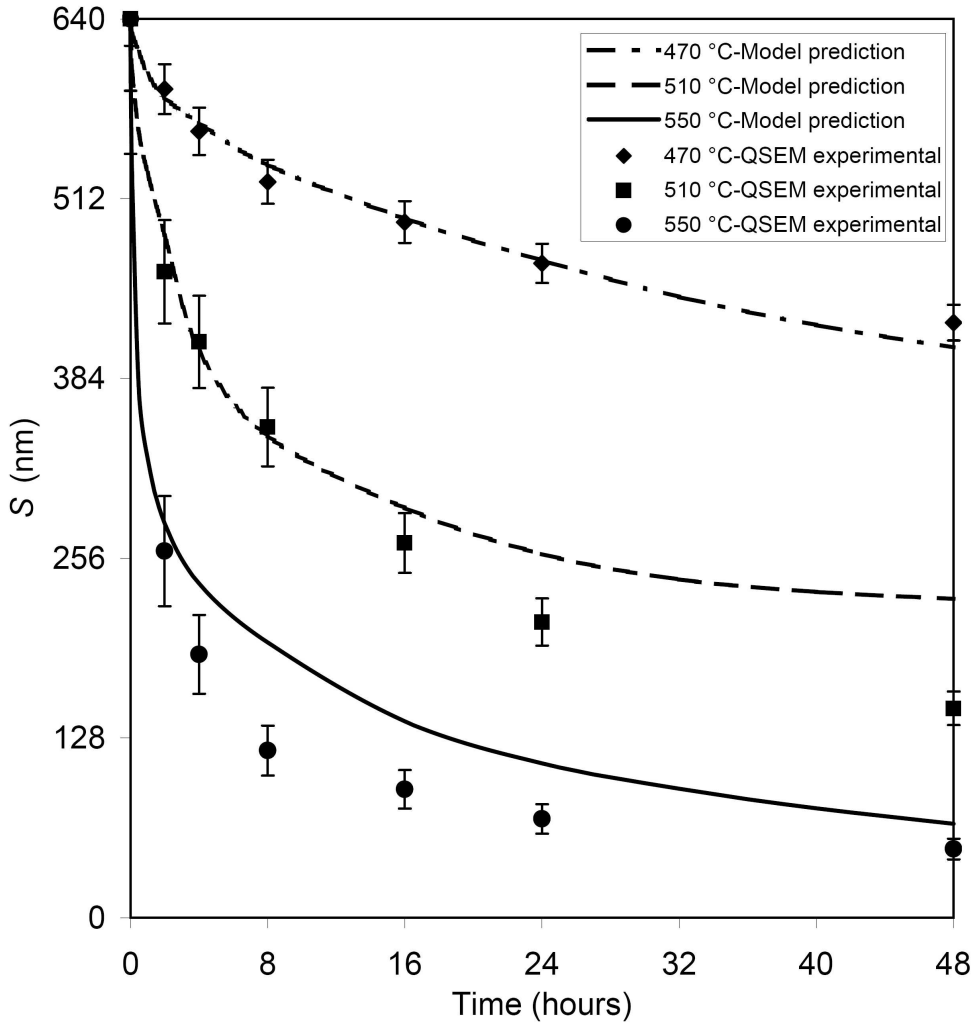

Comparison between the model predictions of the thickness of the particles dissolved during homogenization at different temperatures, and the experimental measurements using FEG-SEM.
664x690mm (96 x 96 DPI)

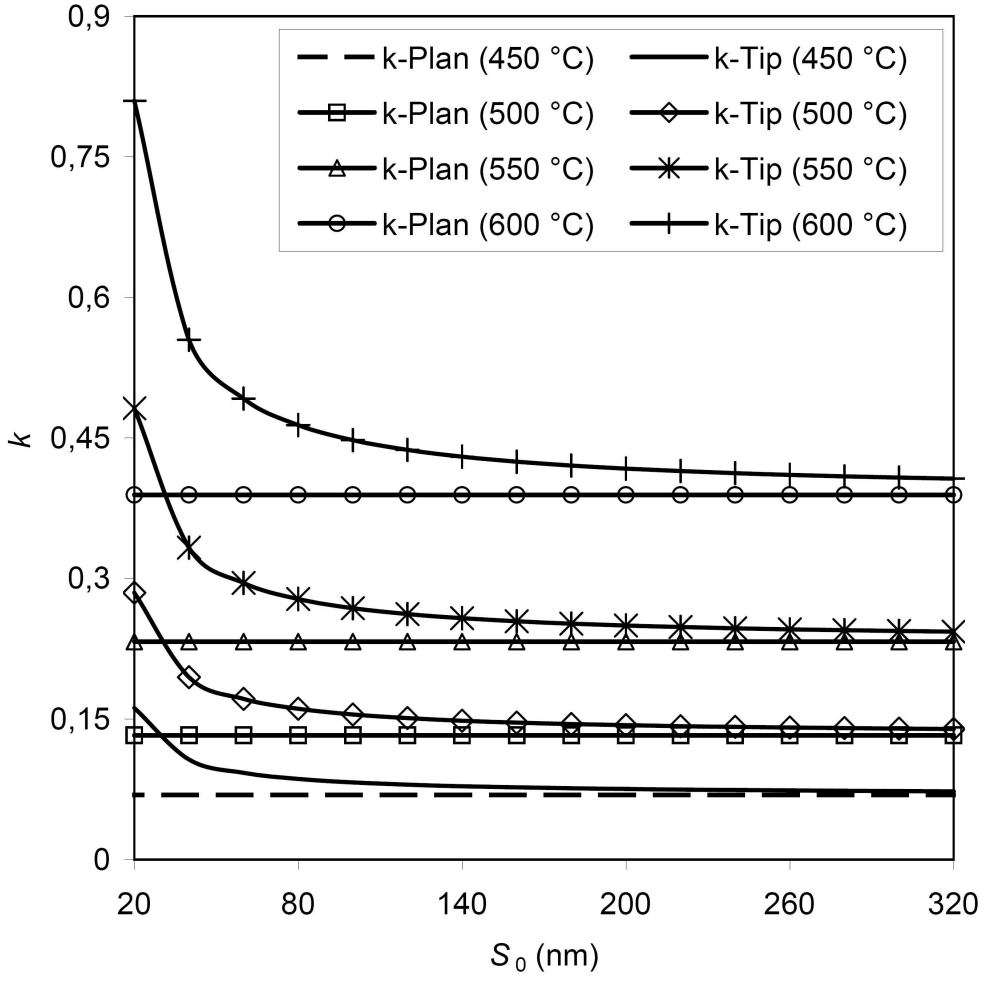

A comparison between the supersaturation parameter of the planar surfaces (kp) and the cylindrical edges (kt) of the particles at different temperatures as a function of the initial width of the particles.
728x732mm (96 x 96 DPI)

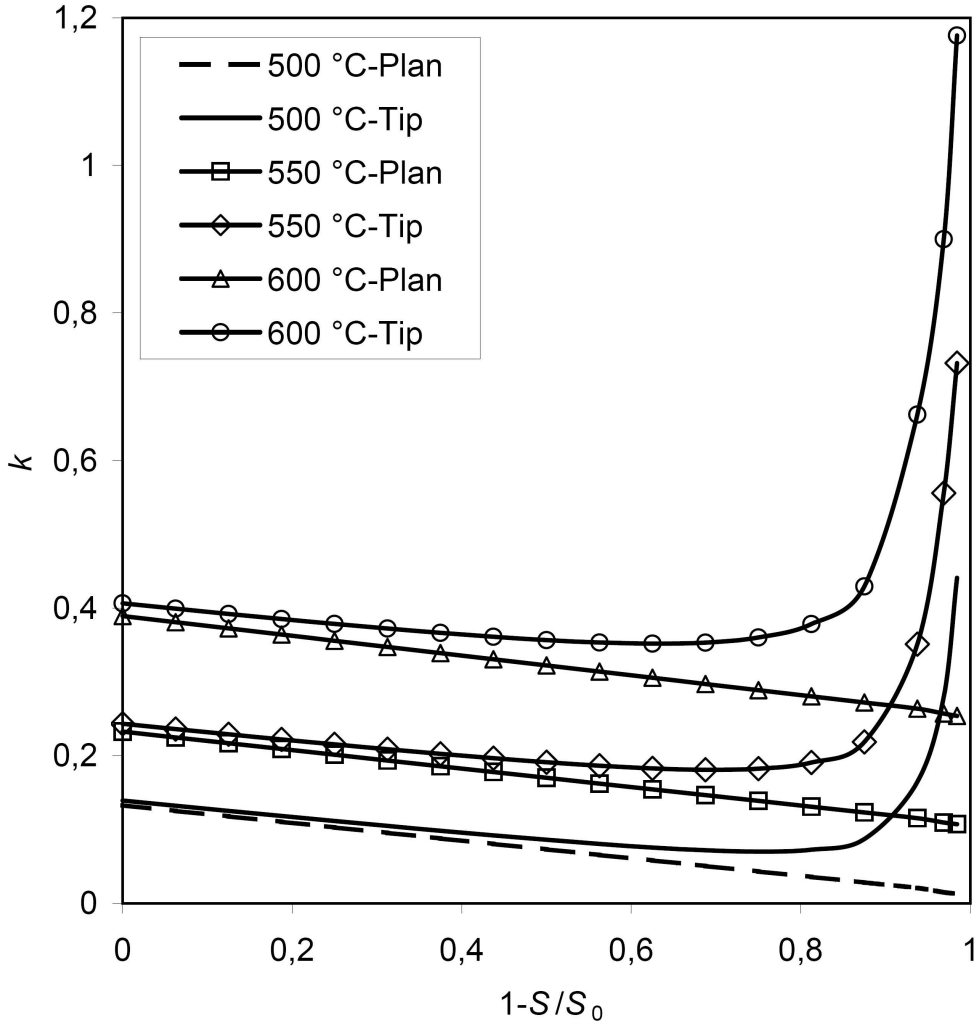

A comparison between the supersaturation parameter of the planar surfaces (kp) and the cylindrical edges (kt) of the particles at different temperatures as a function of the width fraction of the particles dissolved (1-S/S0).
694x730mm (96 x 96 DPI)

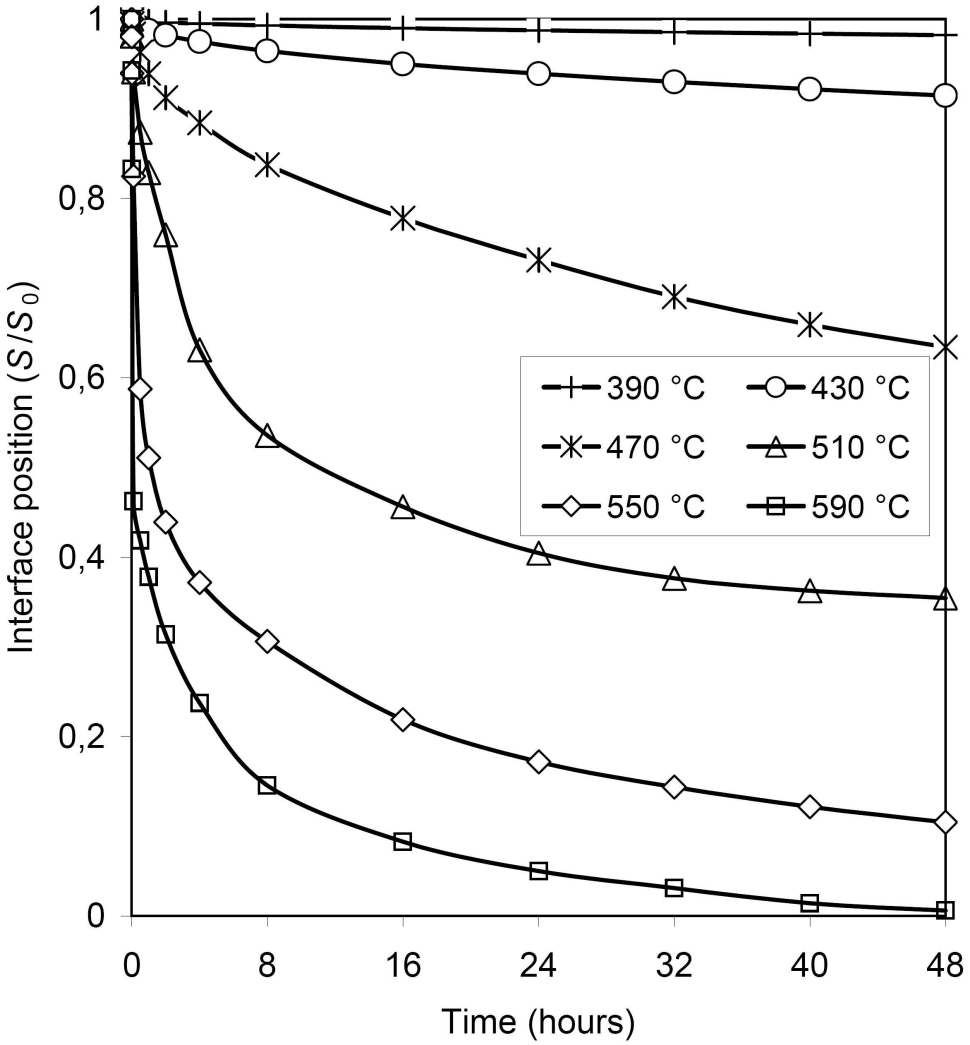

(a) The interface position of the planar surface of the particle and (b) The interface position of the cylindrical edges of the particle.
640x688mm (96 x 96 DPI)

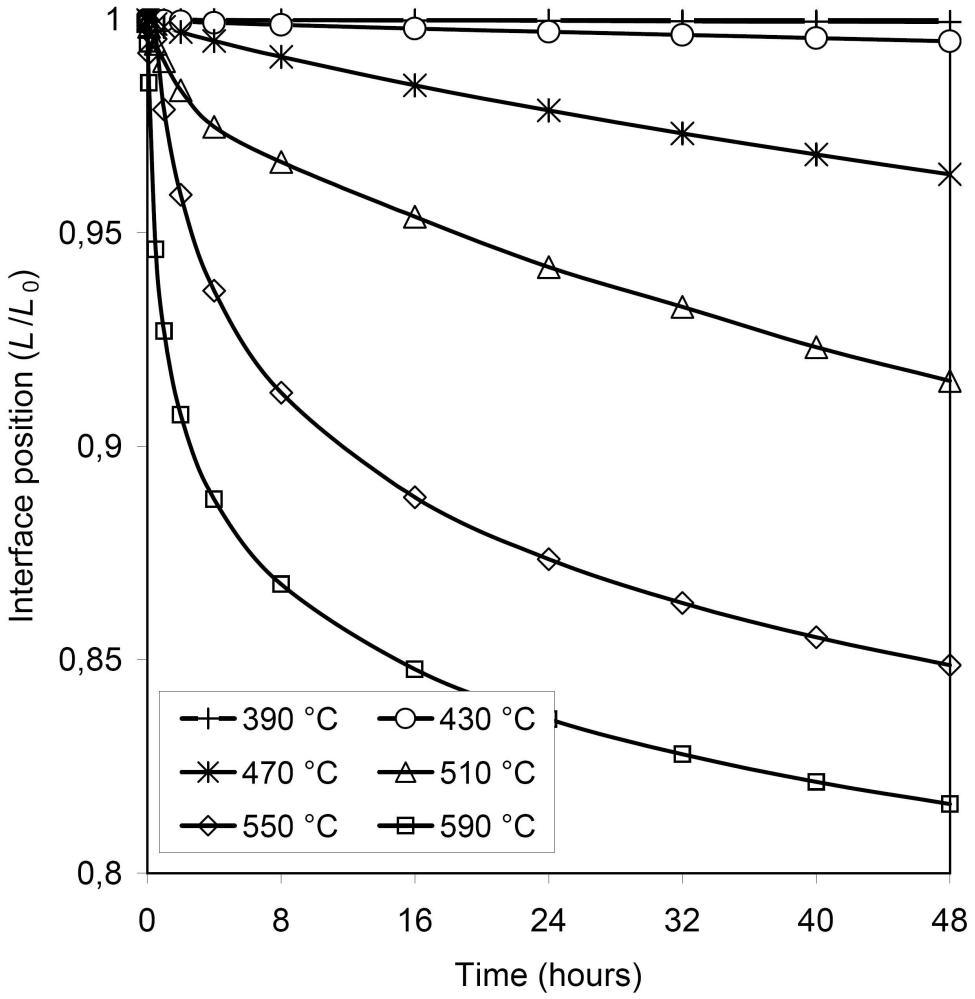

(a) The interface position of the planar surface of the particle and (b) The interface position of the cylindrical edges of the particle.
674x685mm (96 x 96 DPI)

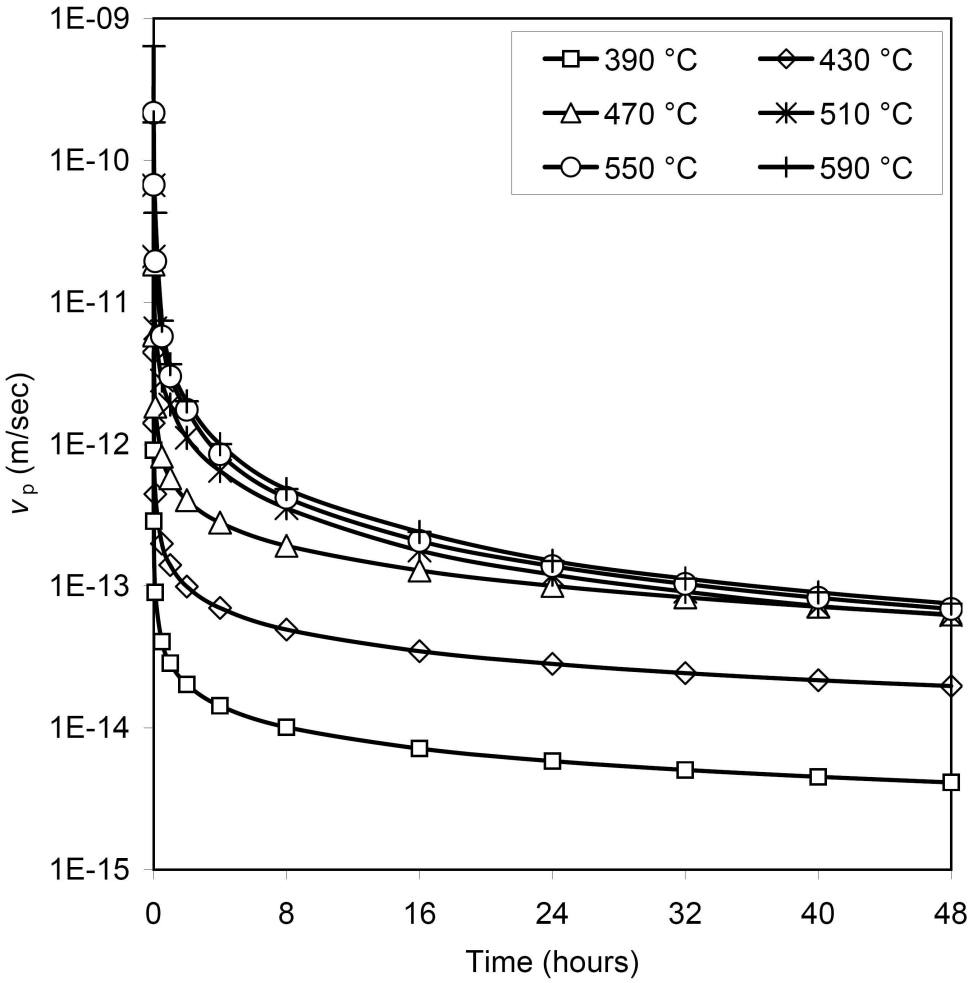

(a) The interface movement rate of the planar surfaces of the particles (vp) and (b) The interface movement rate of the cylindrical edges of the particles (vt).
736x743mm (96 x 96 DPI)

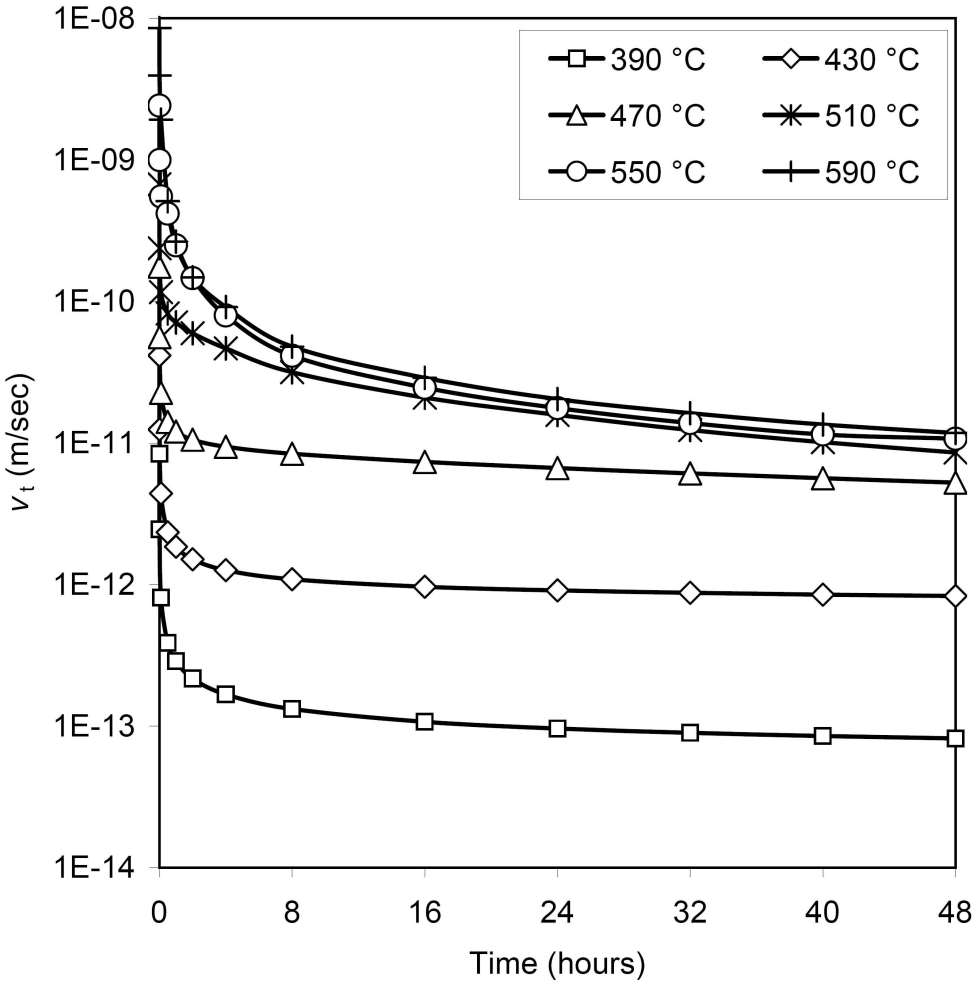

(a) The interface movement rate of the planar surfaces of the particles (vp) and (b) The interface movement rate of the cylindrical edges of the particles (vt).
725x728mm (96 x 96 DPI)

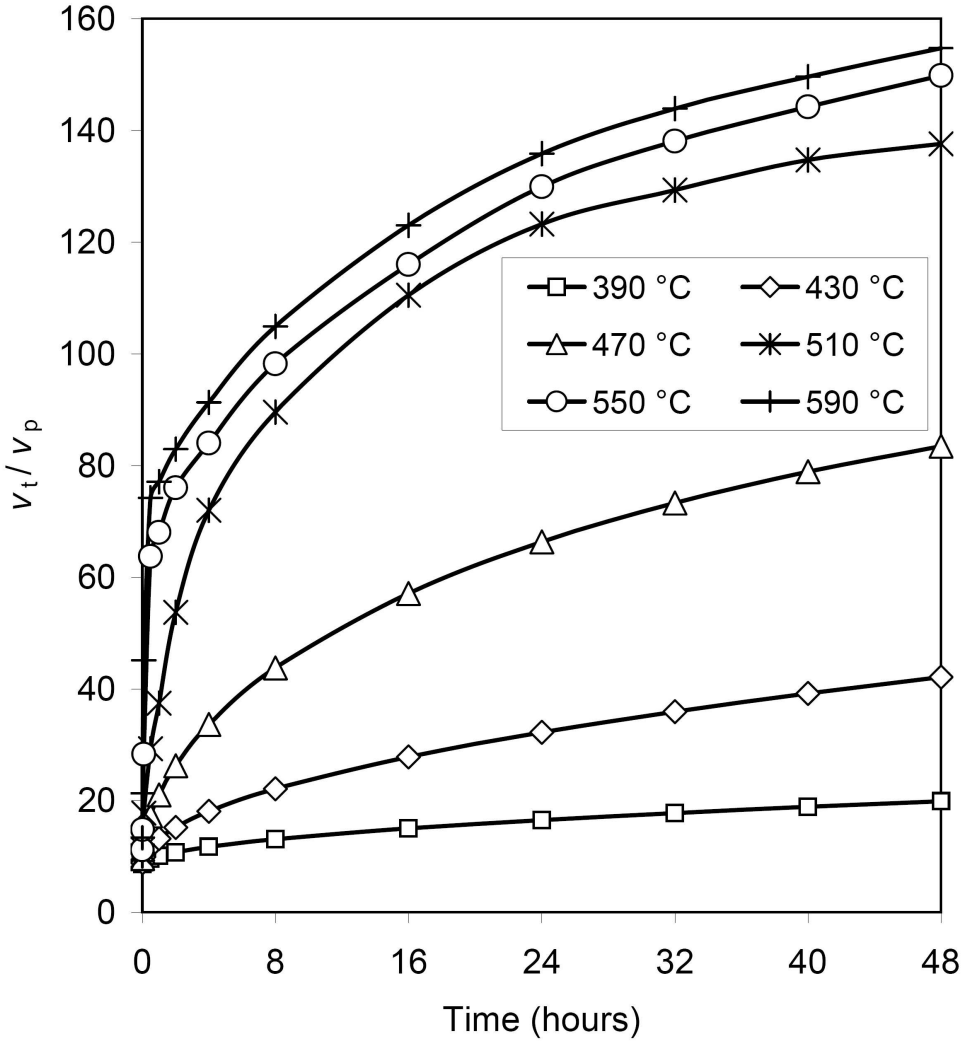

The ratio of the interface movement rate from the cylindrical edges to that from the planar surfaces (vp / vt).
639x686mm (96 x 96 DPI)

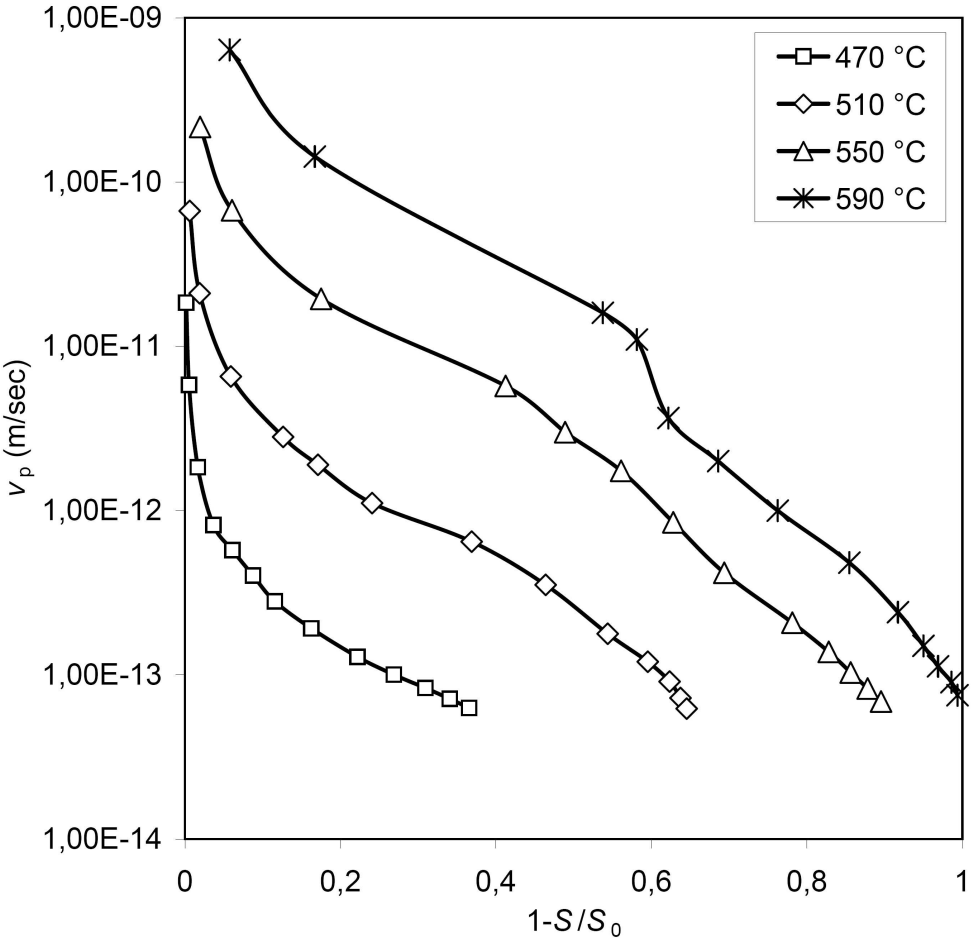

The dependence of the interface movement rate of the (a) planar surfaces (vp) and (b) the cylindrical edges (vt) on the width fraction of the particles dissolved (1-S/S0) at different temperatures. The y axis is shown in a logarithmic scale.
739x705mm (96 x 96 DPI)

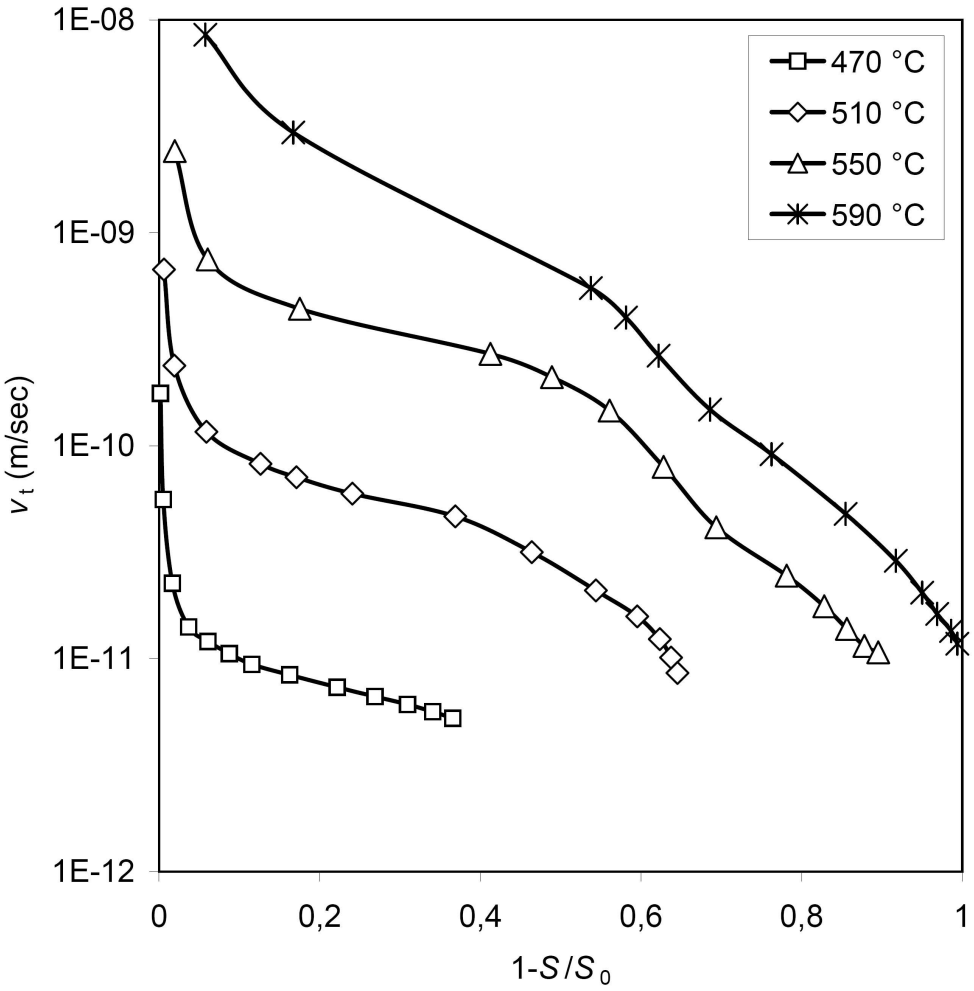

The dependence of the interface movement rate of the (a) planar surfaces (vp) and (b) the cylindrical edges (vt) on the width fraction of the particles dissolved (1-S/S0) at different temperatures. The y axis is shown in a logarithmic scale.
700x702mm (96 x 96 DPI)

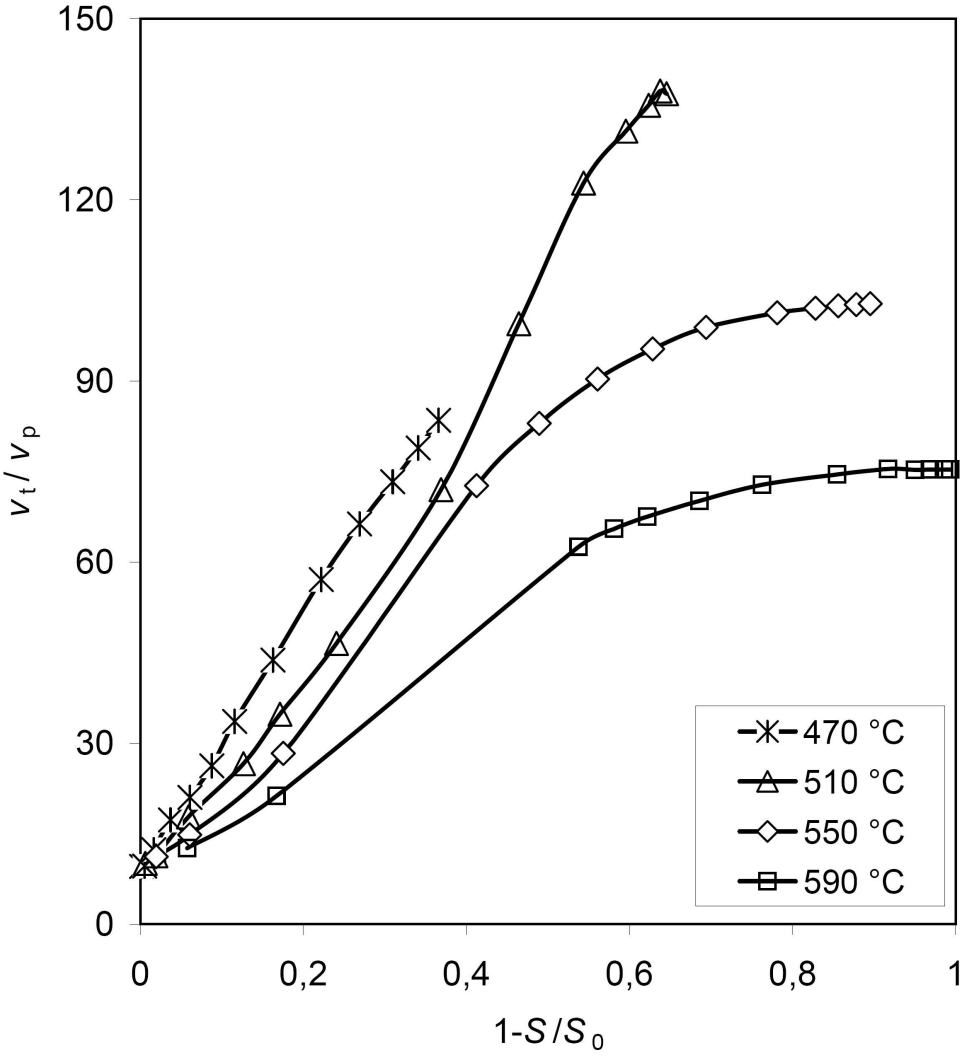

The ratio of the interface movement rate from the cylindrical edges to that from the planar surfaces (vp / vt) as a function of the width fraction of the particles dissolved (1-S/S0) at various homogenization temperatures.
638x690mm (96 x 96 DPI)

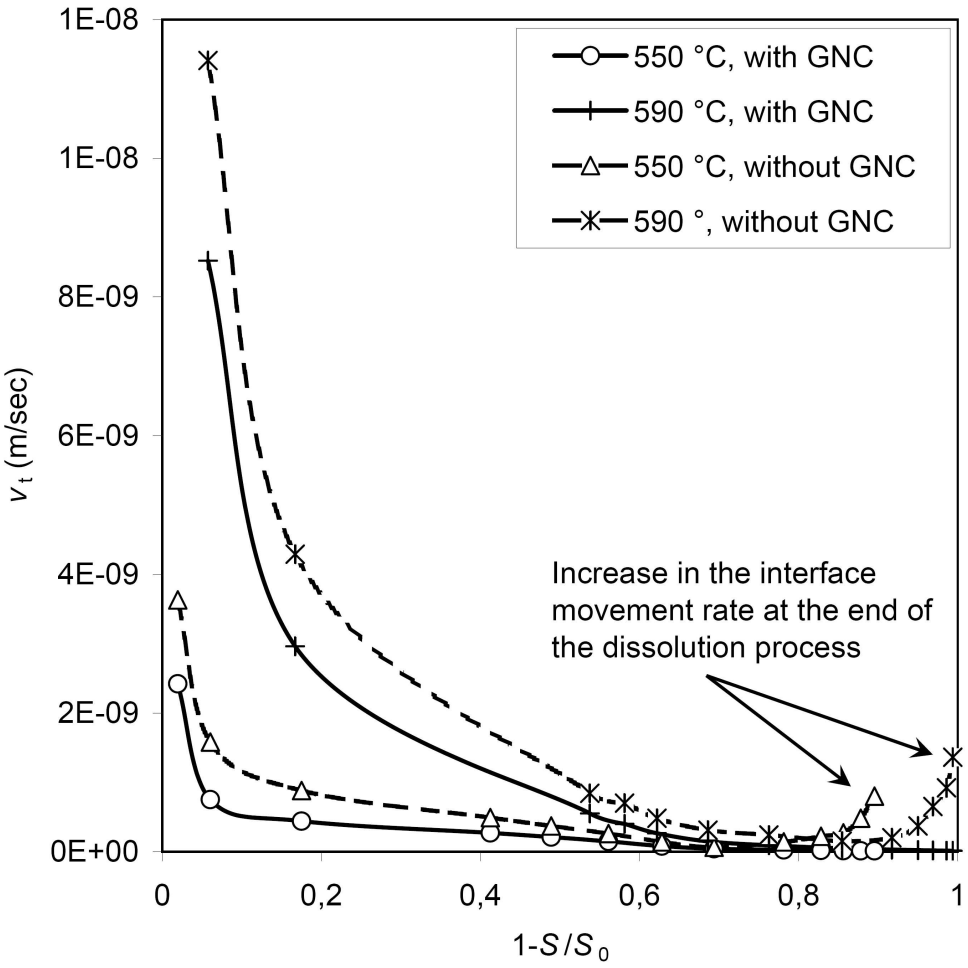

The effect of the geometrically necessary condition (GNC) on the interface movement rate of the cylindrical edges (vt).
742x738mm (96 x 96 DPI)

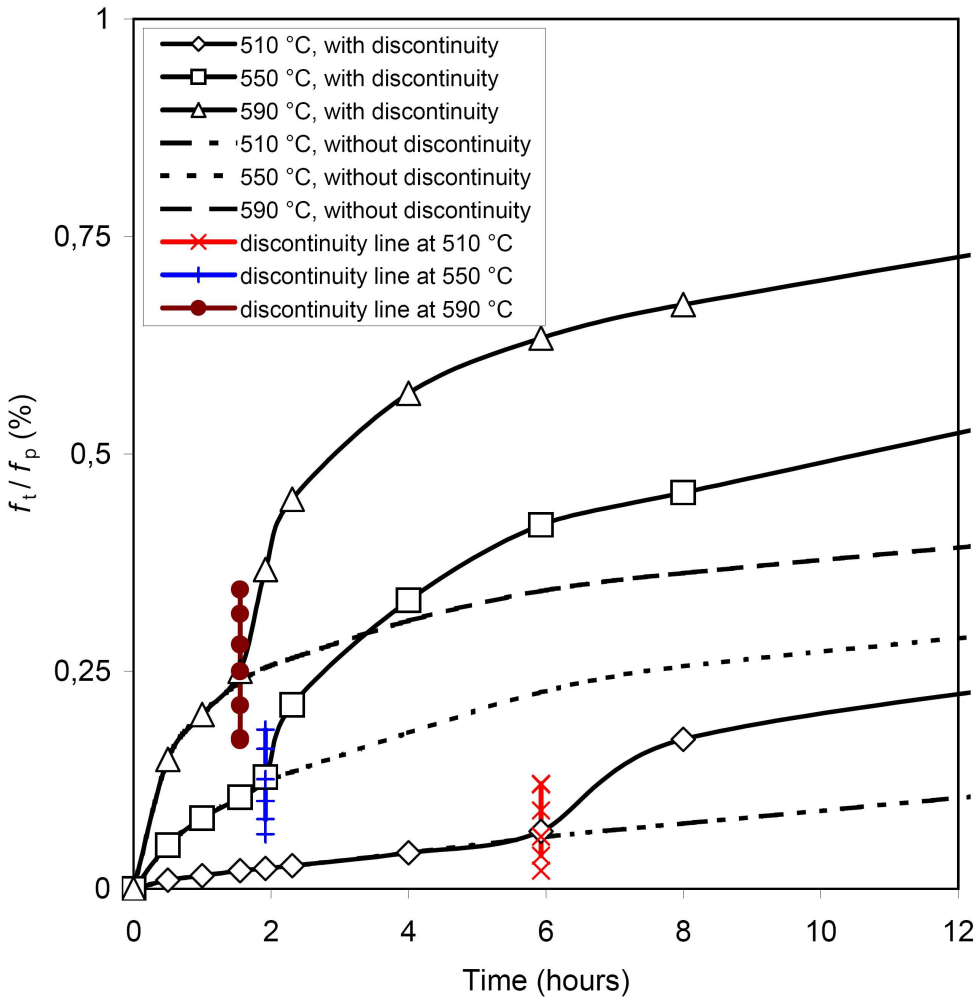

The ratio of the volume fraction of the particles dissolved from the cylindrical edges to that from the planar surfaces (fp / ft), with the effect of the occurrence of the discontinuities taken into consideration. The times of occurrence of discontinuities have been also shown on the figure with vertical lines.
696x704mm (96 x 96 DPI)

Element	Si	Fe	Cu	Mn	Mg	Zn	Ti	Cr	Zr	Al
Wt %	0.30	0.30	0.19	0.35	1.20	4.37	0.002	0.10	0.13	Bal.

Chemical composition of the alloy used in this study
152x13mm (96 x 96 DPI)

Element	Al	Fe	Mn	Si	Zn	Cu
EDX	72.1	16.1	2.8	4.3	2.7	2.0
XRD	62.2	24.2	6.0	7.6		

Measured mean compositions (wt %) of the grain boundary constitutive particles in the as-cast material together with the calculated chemical compositions of the suggested phase identity based on the XRD analysis.
439x132mm (96 x 96 DPI)